Università degli Studi di Padova

SCUOLA DI SCIENZE
DIPARTIMENTO DI FISICA E ASTRONOMIA
“GALILEO GALILEI”

LAUREA MAGISTRALE IN ASTRONOMIA

TESTING MODIFIED GRAVITY WITH THE SUNYAEV ZEL’DOVICH EFFECT

Relatore: Dott. Ric. Michele Liguori
Correlatore: Andrea Ravenni

Laureando:
Vikram Upadhyay
Matricola: 1134068

Anno Accademico 2016 - 2017

To my parents

Contents

Chapter 1

Introduction

Cosmological observations carried out in the last two decades predict the existence of "Dark Energy", an unknown energetic force that strongly influences the current dynamics of our universe. The Planck satellite [38] recently measured the anisotropies in the Cosmic Microwave Background (CMB). Analysis of these anisotropies, along with the Hubble diagram of type Ia Supernovae [39] suggests us that the universe is expanding, with the rate of its expansion growing with time, and also that it is spatially almost flat. This picture is also confirmed by the data from Large Scale Structures (LSS) surveys, that map the distribution of cosmic structures at different redshifts and angular scales.

In an effort to explain the observations, the ΛCDM model was developed in the theoretical framework of General Relativity, based on the Cosmological Principle. This model postulates the existence of a cosmological constant Λ, which is expected to drive the measured cosmic acceleration. We postulate the cosmological constant to account for almost 70% of the energy content of our universe, which is currently unknown. However, due to our lack of evidence so far regarding the existence of dark energy, we cannot rule out other possible explanations for the cosmic acceleration, from both a theoretical and an observational point of view. As such, we can divide the scenarios beyond the ΛCDM into two sides: dark energy (DE) models, in which a time-evolving scalar-field drives the current dynamics of the universe, and modified gravity models (MG), which propose some modifications to Einstein's General Relativity acting on large scales.

In this thesis, we present a method to test modified-gravity models. Growth of large-scale structures is directly related to the governing gravity theory. Any modification to the General Relativity equations, suggested by modified gravity models, will have an affect on the growth of the structures. This change in the dynamics of formation of structures can be tested using tools of cosmological probe, like the Sunyaev-Zel'dovich (SZ) effect. When a low-energy CMB photon travels through the intracluster medium (ICM), it receives an average boost of energy after collisions with the high energy cluster electrons. This effect is known as the SZ effect, and the distortion of the CMB spectrum that it causes can be measured, giving us a tool to probe dense clusters of galaxies. Hence, we can constrain the signals of modified gravity by looking at its predicted SZ power spectrums.

In this thesis we consider a particular class of modified gravity models called the $f(R)$ models. We use the popular Hu-Sawicki parameterization to describe

our $f(R)$ model. We look at the modifications made by this gravity to the halo model, specifically the halo mass function, which describes the distribution of halos by mass and redshift in our universe. We use this modified halo model to compute the 1-halo and 2-halo terms of the thermal-SZ power spectrum. By comparing it to the power spectrum in GR gravity, we are able to constrain the parameters of the $f(R)$ model, and provide forecasts to measure the $f(R)$ signal in future experiments.
In Chapter 2 we provide a general introduction about the standard ΛCDM cosmological model and in Chapter 3, we discuss some observational evidences for some form of dark energy. We discuss the hypothesis of a cosmological constant and then we briefly review possible alternative explanations to the current accelerated expansion of the universe. In Chapter 4 , we describe the physical mechanisms leading to the SZ effect. We discuss the halo model in the context of spherical collapse, with its components: halo mass function, halo bias, and pressure profile. We finally discuss the thermal-SZ autocorrelation power spectrum to be used in our thesis to find a signature for $f(R)$ gravity. In Chapter 5, we outline the theoretical background about the $f(R)$ modified gravity theory, also discussing the *chameleon mechanism* that lets us reproduce General Relativity results on small scales. We also present the modification to the halo model in $f(R)$ gravity, with the fitting functions used in our thesis to compute our results. In Chapter 6, we present our results of modified critical density, halo mass functions, and finally the modifications in the tSZ power spectrums as a function of $f(R)$ theory parameters. In Chapter 7, we do a Fisher forecast of our results to be detected as signal in upcoming experiments like PIXIE and PRISM. Chapter 8 is dedicated to conclusions and outlook.

Chapter 2

ΛCDM Model & FLRW Cosmology

The Λ-Cold Dark Matter (ΛCDM) standard model of cosmology is one of the most successful theories in physics, as it has been supported by a number of cosmological observations. The ΛCDM model is based on the Cosmological Principle and assumes Einstein's General Relativity as the gravity theory acting on all scales. It predicts a universe which started with a "Big Bang", a state characterized by infinite density and temperature. This model was primarily supported by the strong discoveries of the Hubble expansion and of existence of the cosmic microwave microwave background radiation. It was later also discovered that the expansion of the universe is accelerating, rather than slowing down, which astonished much of the astrophysics community.

The ΛCDM model has been very successful at explaining all the present cosmological observations, albeit by invoking the existence of two unknown components: the *dark matter* and the *dark energy*. Very little has been found out about the existence and nature of these two mysterious components. We summarize below the distribution of the present energy content of the universe as predicted by the ΛCDM model, according to the Planck mission results :

Baryonic Matter: $\sim 4.9\%$, Ordinary matter, mainly composed of light elements like hydrogen, helium, lithium, that are predicted to have formed during the "Big Bang Nucleosynthesis", a primordial phase of our universe. The observed abundances of these nuclei are confirmed by the predictions from statistical mechanics.

Dark Matter: $\sim 27\%$, Consisting of non-interacting massive particles of non-baryonic nature with a dust like equation of state. Its existence has been theorized to explain the formation of large scale structures. There have been some significant indirect evidences for the its existence in galaxies and clusters of galaxies, like the flat rotational curve of galaxies, and observations of gravitational lensing produced by clusters. However, we have not yet detected dark matter in laboratories or space, despite the scientific effort. As of now, the nature of dark energy remains a mystery.

Dark Energy: $\sim 68.3\%$, This component is even more evasive in its nature than dark matter. We expect it to be a form of energy that acts as a dynamic repulsive force on large scales, so as to explain the accelerating expansion of our universe. Within the framework of GR employed by the ΛCDM model, the first-guess candidate would be the cosmological constant (Λ), first introduced by Einstein in his field equations. However, in order to explain the current acceleration of

the universe, we require the value of the energy density associated with Λ to be incredibly small. Alternatively, another explanation could be that Einstein's general relativity fails on cosmological scales, and there might not be any mysterious "dark matter", after all.
The standard model of cosmology depends heavily on our limited knowledge of the full nature of gravity. General Relativity has not been tested independently on galactic and cosmological scales. Perhaps, we might have to revise the theory of gravity on cosmological scales and the standard model of cosmology, to explain the late time acceleration of our universe.

2.1 FLRW metric

The Cosmological Principle was first formulated by Albert Einstein and it represents the foundational hypothesis of cosmology [42]. It states: "On sufficiently large scales, the universe is both homogeneous and isotropic". Homogeneity is the property of being identical everywhere in space, while isotropy is the property of things looking the same in every direction.
Observations of the Large Scale Structure of the universe validate the property of homogeneity, in a statistical sense. The universe can be considered identical, on average, in different places if we look at sufficiently large patches > 200 Mpc. The strongest evidence for isotropy is given by observation of the Cosmic Microwave Background Radiation.
The Cosmological Principle was introduced before there was any observational evidence, and it has been present in various forms in all the cosmological theories from the last century, from the Big Bang to the Steady State Model. This states its significance in cosmology.
In relativistic cosmology, the cosmological principle allows us to simplify many of Einstein's complicated non-linear equations by providing symmetries. Since a symmetry implies a conservation rule, any three-dimensional spatial slice of the space-time has to be invariant both under translations and rotations, in order to satisfy the Cosmological Principle.
General Relativity employs a metric tensor $g_{\mu\nu}$ to describe the geometric properties of space-time by providing us a way to measure physical distances in curved manifolds. The most general metric for a space-time, characterized by maximally symmetric space-like hypersurfaces, is described by the Friedmann-Lemaître-Robertson-Walker (FLRW) line element:

$$ds^2 = -dt^2 + a^2(t)[\frac{dr^2}{1 - Kr^2} + r^2(d\theta^2 + sin^2\theta d\phi^2), \tag{2.1}$$

where we adopt, the conventional signature (-,+,+,+). The coordinates r, θ and ϕ are comoving coordinates.
Let's assume that the universe is a fluid in which the fundamental particles are galaxies, and a fluid element has a volume that contains many galaxies. A freely moving fluid element is at rest in the comoving coordinate system, and all the observers who are at rest with the local freely moving fluid element are called "fundamental observers".
The function $a(t)$, relating the comoving coordinates to physical distances, is called the *scale factor*. It is normalized in a way that it's unity in our present universe. The scale factor varies in time, changing the overall size of the observable

universe while preserving isotropy and homogeneity. Based on the cosmological principle, a fundamental observer sees the same picture of the universe in every direction, but this picture can change with time depending on the evolution of $a(t)$.
The constant K describes the curvature of space-like hypersurfaces: K $= 0$ corresponds to a flat three-dimensional space with no curvature; K > 0 corresponds to a positive curvature, or a closed space; and K < 0 corresponds to a negative curvature i.e., an open space. The curvature is related to the energy content of the universe, as we will show in the next section.

2.2 Evolution Equations

The dynamics of the evolution of our universe can be fully determined by the temporal evolution of the scale factor. To obtain $a(t)$, we begin with writing the Einstein equations using the FLRW metric:

$$G^\mu_\nu = R^\mu_\nu - \frac{1}{2}Rg^\mu_\nu = 8\pi G T^\mu_\nu. \tag{2.2}$$

Einstein field equations describe gravitation to be a consequence of interplay between the energy content and the geometry of the space-time. The Ricci tensor R^μ_ν and the Ricci scalar R describe the geometric properties of space-time and depend on the metric and its derivatives, whereas T^μ_ν is the energy-momentum tensor describing the energy content of the universe. Employing the cosmological principle, we assume the universe to be filled by perfect fluids, for which the energy-momentum tensor assumes the following form in any reference frame:

$$T^\mu_\nu = (p+\rho)u^\mu u_\nu + pg^\mu_\nu, \tag{2.3}$$

where u^μ is the four-velocity of the fluid, p and ρ are the pressure density and the energy density of the fluid, respectively. In the comoving coordinate system, in which the fluid is at rest, the four velocity: $u^\mu = (1, 0, 0, 0)$, thus T^μ_ν is simply:

$$T^\mu_\nu = Diag(-\rho, p, p, p). \tag{2.4}$$

Computing the Ricci tensor and Ricci scalar for a FLRW background, we get:

$$\begin{aligned} R^0_0 &= 3\frac{\ddot{a}}{a}, \\ R^i_j &= (3\frac{\ddot{a}}{a} + 2\frac{\dot{a}^2}{a^2} + 2\frac{K}{a^2})\delta^i_j, \\ R &= 6(\frac{\ddot{a}}{a} + \frac{\dot{a}^2}{a^2} + \frac{K}{a^2}). \end{aligned} \tag{2.5}$$

For an isotropic and homogeneous universe, substituting the value of g^μ_ν, R^μ_ν, R, and T^μ_ν into the Einstein equations gives us:

$$H^2 \equiv (\frac{\dot{a}}{a})^2 = \frac{8\pi G}{3}\rho - \frac{K}{a^2} \tag{2.6}$$

$$\frac{\ddot{a}}{a} = -\frac{4\pi G}{3}(\rho + 3p). \tag{2.7}$$

These are known as the *Friedmann equations.* These two differential equations govern the background dynamics of the universe, and relate the evolution of the

scale factor $a(t)$ with $p(t)$ and ρ(t). The Friedmann equations reveal that there is a direct connection between the density of the universe and its global geometry. The factor $H(t) \equiv \frac{\dot{a}}{a}$, is called the Hubble rate and describes the rate of the cosmic expansion.
For a given rate of expansion, there is a critical density that yields a null spatial curvature K = 0:

$$\rho_c = \frac{3H^2}{8\pi G}. \tag{2.8}$$

Using this, one can rewrite Eq. (2.6) as below:

$$\Omega - 1 = \frac{K}{(aH)^2} \tag{2.9}$$

where $\Omega \equiv \rho/\rho_c$ is the dimensionless density parameter. From the equation above, we can see that:

$$\begin{aligned} &\Omega > 1 \ or \ \rho > \rho_c \rightarrow K > 0, \\ &\Omega = 1 \ or \ \rho = \rho_c \rightarrow K = 0, \\ &\Omega < 1 \ or \ \rho < \rho_c \rightarrow K < 0. \end{aligned}$$

Observations have shown that Ω_{tot} is very close to 1, implying a spatially flat geometry. This is a natural result of an inflationary phase in the primordial universe [40].
From the Bianchi identity ($\Delta_\mu T^\mu_\nu = 0$), we get the continuity equation:

$$\dot{\rho} = -3H(\rho + p). \tag{2.10}$$

This equation expresses the conservation of energy for fluids in FLRW space-time. It is important to note that the continuity equation can also be obtained from the Friedmann equations by eliminating the scale factor. Indeed, the continuity equation together with the Friedmann equations, form a set of three mutually-dependent equations with the variables: $a(t)$, $p(t)$, ρ(t).
To obtain the solution, we require a relation between the density and the pressure, called an *equation of state* (EoS). In many cases of physical interest, the equation of state is a simple linear law:

$$p = \omega \rho, \tag{2.11}$$

where ω is a proportionality constant.
According to the current picture, the universe is filled by a mixture of different energetic components, each one with its own EoS. The case with $\omega = 0$ represents pressure-less material, called dust. The *dust* equation of state is a good assumption for fluid of all the non-relativistic particles, like nuclei and electrons of ordinary matter and the cold/non-baryonic dark matter particles, since they exert a pressure of order $K_B T$, which is negligible with respect to their energy of order mc^2. On the other hand, a fluid of radiation, made of non-degenerate and ultra-relativistic particles like photons or neutrinos, exert non-negligible pressure. In thermal equilibrium, they have an equation of state: $\omega = 1/3$.
Let's also consider the case of a fluid with ω = -1. This case refers to a so called *cosmological constant* Λ. As we will see in the next sections, a fluid called the *Dark Energy* with ω close to -1 is supposed to dominate the current dynamics of the universe and drive the cosmic accelerated expansion. As such, the dark energy component is identified with an exact cosmological constant in the framework of

ΛCDM model.
For a single perfect fluid with EoS ω, the solution to the continuity equation gives:

$$\rho \propto a^{-3(\omega+1)}. \tag{2.12}$$

universe The total energy density on the right hand side of Eq. (2.6), receives contributions from all the components present in the universe, each evolving differently with time. As we know, the main energetic components consist of: non-relativistic particles, like baryonic matter and dark matter (with density ρ_m); relativistic particles, like photons and neutrinos (with density ρ_{rad}), and dark energy (with density ρ_{DE}).
According to the ΛCDM model, the universe undergoes different phases, during which different components dominate the dynamical evolution of the scale factor. Considering a null spatial curvature (K = 0), we can combine the solutions of Eq. (2.6) and Eq. (2.10) during these phases as follows:

$$\begin{aligned} Radiation\ dominated: a(t) \propto t^{\frac{1}{2}},\ \rho(a) \simeq \rho_{rad}(a) \propto a^{-4}, \\ Matter\ dominated: a(t) \propto t^{\frac{2}{3}},\ \rho(a) \simeq \rho_m(a) \propto a^{-3}, \\ \Lambda\ dominated: a(t) \propto e^{Ht},\ \rho \simeq \rho_\Lambda = const. \end{aligned} \tag{2.13}$$

Finally, using the above results, we can express the Hubble parameter in ΛCDM model as follows:

$$\begin{aligned} H^2 = (\Omega^{(0)}_{rad} a^{-4} + \Omega^{(0)}_m a^{-3} + (1 - \Omega^{(0)}) a^{-2} + \Omega^{(0)}_\Lambda) H_0^2, \\ \Omega^{(0)} = \Omega^{(0)}_{rad} + \Omega^{(0)}_m + \Omega^{(0)}_\Lambda \end{aligned} \tag{2.14}$$

where the Ω-parameters are the dimensionless density parameters of the various energetic component, defined as $\Omega_i = \rho_i/\rho_c$, and the superscript (0) indicates that quantities have to be evaluated at the present epoch.

2.3 Hubble expansion

A fundamental evidence supporting the validity of the FRLW model is that the light coming from objects far away in space is Doppler shifted. This is interpreted as a relative velocity away from Earth. In 1929, Hubble observed some nearby galaxies and found that the distance d of an emitting source, and the shift in its spectral lines followed a linear relation: $z = \frac{\Delta\lambda}{\lambda}$ on scales of order > 10 megaparsecs (Mpc):

$$cz \sim v = H_0 d, \tag{2.15}$$

where H_0 is called the *Hubble constant*, identified as the Hubble parameter evaluated at the present epoch.
The recession velocity, v, of a cosmological source can be deduced from the redshift z by the relation:

$$z = \frac{\lambda_0}{\lambda_e} - 1 = \sqrt{\frac{1 + v/c}{1 - v/c}} - 1 \sim \frac{v}{c} \tag{2.16}$$

Here, λ_0 and λ_e are the observed and emitted wavelengths respectively. However, the last equality is valid only in the limit v ≪ c (small distances). To account for sources at large distances, we should relate this effect to a relativistic temporal

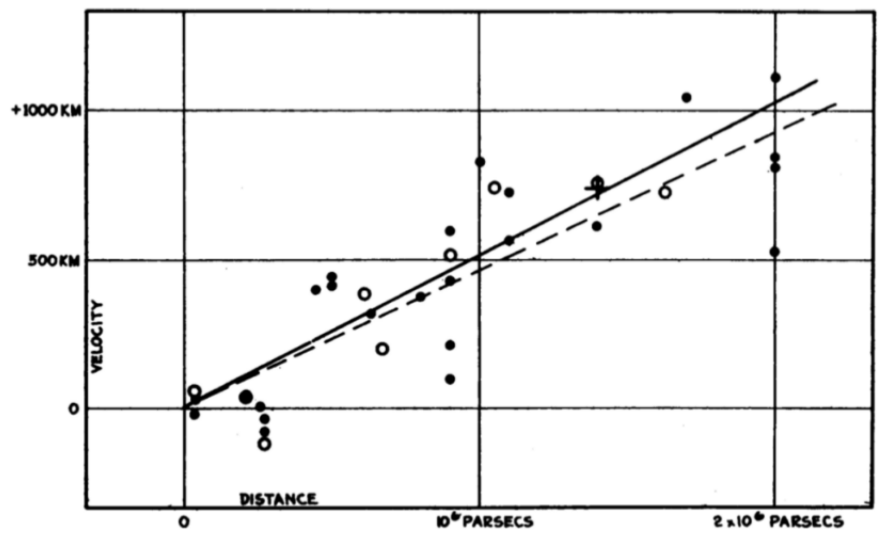

Figure 2.1: The original Hubble diagram [41]

dilation, which affects the frequencies of photons traveling through an expanding space-time. We can show that the observed frequency of a photon, changes proportionally to the scale factor, making it possible to relate the redshift to the scale factor as follows:

$$1 + z = \frac{1}{a}. \tag{2.17}$$

This tells us that redshift is a measure of the scale factor of the universe at the time when radiation was emitted by the source.
The evidence for an expanding universe confirms the Friedmann world model, which led physicists to refuse the Steady State model that prescribed a static universe. Something worth noting is that the notion of distance in expanding space-time differs from the euclidean case, hence one should pay attention to the distance appearing on the right hand side of Eq. (2.15).
We can define the proper distance from the FRLW line element as [42]:

$$d_p = a(t) \int_0^r \frac{dr}{\sqrt{1 - Kr^2}} = a(t)\chi. \tag{2.18}$$

where χ is the comoving distance i.e., the distance between two points measured along a path defined at the present cosmological time ($a = 1$). The comoving distance does not change for two astronomical objects whose motion is just due to the cosmic expansion.
We can relate the comoving (and proper) distance to the source's redshift using the fact that the observer (at the present time t_0) and emitter (at time t) are connected by a light ray along a radial path ($ds^2 = 0$), which gives us the following equalities:

$$\chi = \int_0^r \frac{dr}{\sqrt{1 - Kr^2}} = \int_t^{t_0} \frac{cdt'}{a(t')} = \int_a^1 \frac{cda'}{a'^2 H(a')} = \int_0^z \frac{cdz'}{H(z')} \tag{2.19}$$

where we used Eq. (2.17) and the definition of Hubble parameter. We note that for objects at rest in comoving coordinates, the Hubble law of Eq. (2.15) can be obtained in terms of proper distance by differentiating Eq. (2.18) with respect to

time.
Light emitted by distant objects takes a finite time to reach us. Therefore, we cannot make measurements along a surface of constant proper time, but only along our past light cone. This deems the proper distance of little operational significance. However, we can define other kinds of distances which are, in principle, directly measurable.
For an object of intrinsic luminosity L, the measured energy flux F defines the luminosity distance d_L to the object to be:

$$d_L \equiv \sqrt{\frac{L}{4\pi F}} \tag{2.20}$$

The luminosity distance generalizes the inverse square law, valid for a Minkowski space-time, to an expanding universe: $F = L/(4\pi d^2)$. In an expanding space-time, this observed flux is reduced by a factor of $(1+z)^2$ as it is proportional to the energy transfer rate : one power of $(1+z)$ comes from reduced energy due to wavelength lengthening of the emitted light, and another due to the increased time interval. Thus, in terms of comoving distance, we get:

$$\begin{aligned} F =& \frac{L}{4\pi\chi^2(1+z)^2}, \\ d_L =&(1+z)\chi = (1+z)\int_0^z \frac{cdz'}{H_0\sqrt{\Omega_m(1+z')^3 + \Omega_{DE}(1+z')^{3(1+\omega)}}} \end{aligned} \tag{2.21}$$

In the last equality, using Eq. (2.19) and Eq. (2.14), we assumed null spatial curvature and neglected the contribution of radiation as we are only interested in low redshift regimes, when the contribution from the dark energy starts to be important. Cosmological models with a Hubble parameter having a different z dependence yield a different distance-redshift relation. Thus, this relation can be used to distinguish between different cosmological scenarios. This makes the above equation crucial for observational cosmology. Practically, we can measure the luminosity distance for a class of sources at different redshifts, and then fit the data with a theoretical curve in a redshift-distance diagram, called the *Hubble diagram*. We see that, when we take the limit of Eq. (2.21) for $z \ll 1$, we recover the Hubble law $cz = H_0 d_L$. The Hubble relation is the functional dependence of distance on the redshift. Hence, the Hubble curve helps in distinguishing between different cosmological scenarios.
As we shall discuss in the next section, our universe was discovered to be in an accelerating expansion phase. In the right panel of Figure 2.2, we see different theoretical Hubble diagrams, based on Eq. (2.21) assuming a spatially flat universe with two main components: matter, and the cosmological constant.

Another distance measure in cosmology is the so called angular diameter distance d_A, defined in terms of the object's proper size l, and the apparent angular size θ of the object as viewed from earth:

$$\begin{aligned} d_A \equiv \frac{l}{\theta}, \\ d_A = \frac{\chi}{1+z} = \frac{d_L}{(1+z)^2}. \end{aligned} \tag{2.22}$$

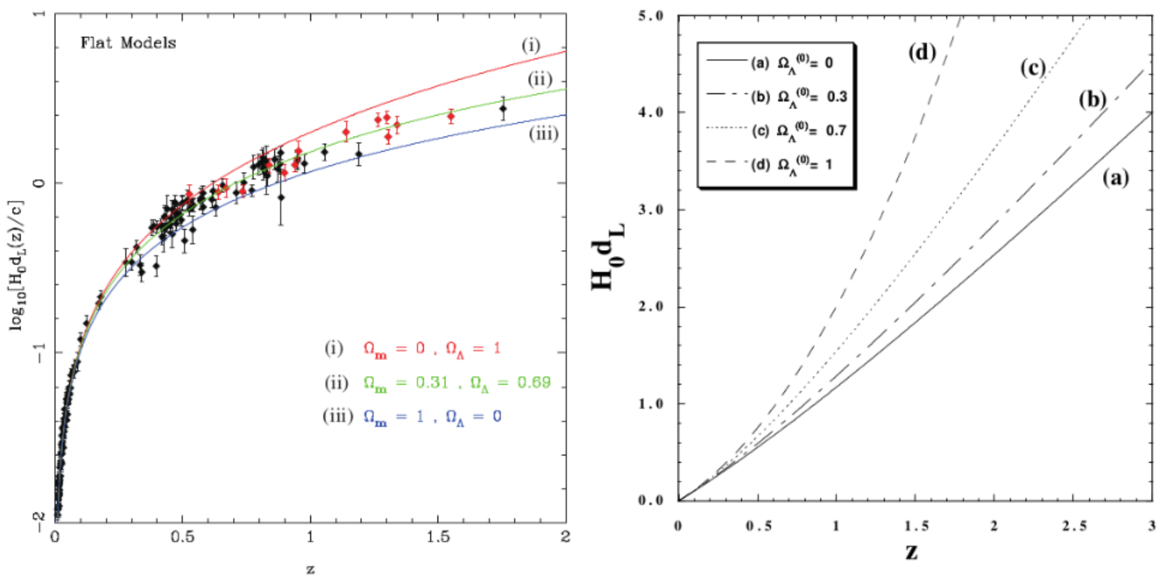

Figure 2.2: **Left**: The luminosity distance $H_0 d_L$ (log plot) versus the redshift z for a flat cosmological model. The black points come from the "Gold" data sets, whereas the red points show the data from HST. Three curves show the theoretical values of $H_0 d_L$ for (i) $\Omega_m = 0, \Omega_{DE} = 1$,(ii)$\Omega_m = 0.31$,$\Omega_{DE} = 0.69$ and(iii)$\Omega_m = 1, \Omega_{DE} = 0$. **Right**: Luminosity distance $H_0 d_L$ for a two component flat universe with a non-relativistic fluid ($\omega_m = 0$) and a cosmological constant ($\omega_\Lambda = -1$). We plot $H_0 d_L$ for various values of Ω_Λ [39]

where the second line of Eq. (2.22) expresses the connection between d_A and the luminosity distance d_L. The $d_A - z$ relation can be used to test cosmology, just like the $d_L - z$ relation.

Chapter 3

The Accelerating universe

Considering the Friedmann equations (2.6-2.7) and imposing an accelerated expansion rate, we get:

$$\ddot{a} = -\frac{4}{3}\pi G(\rho + 3p)a > 0 \Leftrightarrow p < -\frac{1}{3}\rho \Leftrightarrow \omega \equiv \frac{p}{\rho} < -\frac{1}{3}. \tag{3.1}$$

The last equation lets us define the "dark energy", a perfect fluid with EoS satisfying: $\omega < -1/3$, which gives rise to a negative pressure term in the Friedmann equations, leading to $\ddot{a} > 0$.
In this section we will review the most important observational evidences for Dark Energy and introduce the standard model interpretation characterized by a cosmological constant Λ with EoS $\omega = -1$. So far, the cosmological constant fits all the data very well and is the simplest solution available to the cosmic acceleration problem. We expect "Λ" to be there, if only, for the vacuum energy. The issue is that, for the energy associated with the cosmological constant to have the observed value, an incredible fine-tuning is required.

3.1 Supernovae Ia

In the late nineties, astronomers found a class of sources particularly suitable for plotting Hubble diagrams: Type Ia Supernovae. Since these objects have known intrinsic luminosity (or absolute magnitude), they can be used to determine the luminosity distance from measurements of the received flux. For this nature, these sources are known as *standard candles*. For a full review, refer to [43].
Type Ia supernovae (SN Ia) can be observed when white dwarf stars go beyond their Chandrasekhar mass limit ($1.44 M_{\odot}$) and explode. White dwarfs are compact stars made up of Carbon and Oxygen and supported by degenerate electron pressure. Since these stars are often found in binary systems, they can accrete mass from their companion. The mass accreted onto the surface of the white dwarf can raise the surface temperatures high enough to instigate nuclear burning, followed by a deflagration front propagating into the inner layers. Thus, the entire star can explode undergoing a process of thermal runaway.
The formation process of SN Ia should be the same irrespective of their location in the universe, and the cosmic epoch they occur in. This is why they have a common redshift-independent absolute magnitude. There are a number of features that make Type Ia Supernovae precise tools for cosmological investigations:

- they have peculiar light curves with a maximum luminosity corresponding to an absolute magnitude M $\simeq$ 19.4, making them as luminous as a small galaxy.
- they can be easily distinguished in a wide field full of stars since they are rapidly variable sources, with a time scale in the order of ten days.
- they are point-like sources, allowing precise photometric analysis.

These features have allowed us to detect several Type Ia Supernovae and their redshifts have been measured with good precision upto $z \sim 1.5$, providing a direct evidence of the currently accelerating expansion of the universe. The pioneers in the field of analyzing the luminosity distance-redshift relation for were Perlmutter, Riess and Schimdt, who won the Nobel Prize in 2011 for their discoveries. Their observations showed a substantial deviation from the scenario of a matter dominated universe. This was indicated by the fact that their measured luminosities were (on average) considerably less than expected, and the Hubble curve was bent upward (Figure 2.2). Based on a set of 42 Type Ia Supernovae in the redshift range $z = 0.18 - 0.83$ and considering a spatially flat universe with two main component ($\Omega_m^{(0)} + \Omega_\Lambda^{(0)} = 1$), Perlmutter et al. [14] found that $\Omega_m = 0.28^{+0.09}_{-0.08}$ (1σ statistical), thus showing that about 70% of the energy density of the present universe consists of dark energy. In 2004 Riess et al. [13] reported the measurement of 16 high-redshift SN Ia with redshift $z > 1.25$ with the Hubble Space Telescope (HST). By including 170 previously known SN Ia data points, they showed that the universe showed a transition from deceleration to acceleration at $> 99\%$ confidence level. In Figure 2.2 left panel, we show the Hubble diagram established on this dataset.

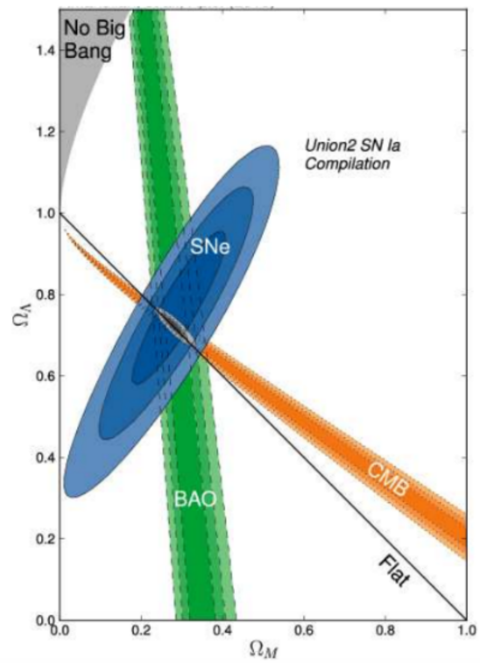

Figure 3.1: The $\Omega_m - \Omega_{DE}$ confidence regions constrained by SN Ia, CMB and galaxy clustering.

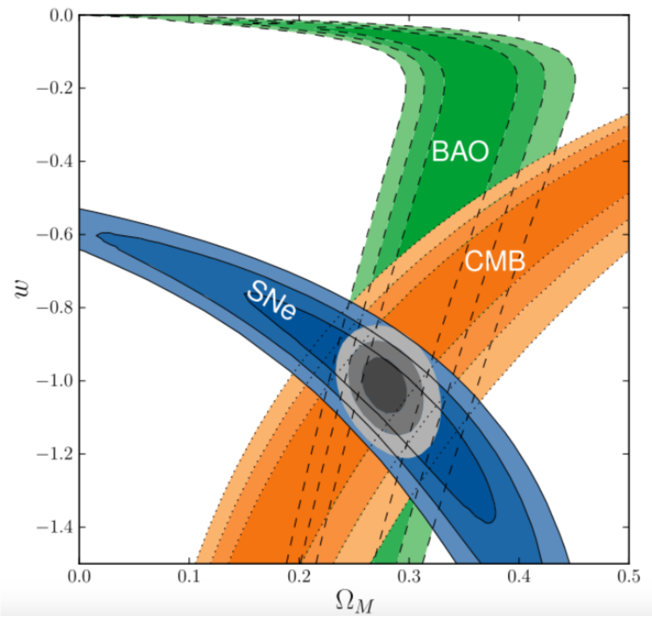

Figure 3.2: The $\omega - \Omega_m$ confidence regions constrained by SN Ia, CMB and galaxy clustering.

3.2 Cosmic Microwave Background

The Cosmic Microwave Background (CMB) is currently the strongest probe of precision cosmology. It places a 1-10% level constraint on a large number of cosmological parameters, including the baryon and cold dark matter densities and the amplitude and tilt of the spectrum of primordial fluctuations. Although its existence was already theorized long ago in the 40's, as a consequence of the Big Bang model, it's first detection in 1965 was a lucky result of Penzias and Wilson's investigation about the sources of atmospheric noise in telecommunication.
The Cosmic Microwave Background photons last interacted with matter at z $\simeq$ 1090 during the recombination epoch. Being a relic radiation from the early stages of our universe, CMB carries information about the hot primordial universe and its subsequent evolution.
The FIRAS spectrophotometer of the COBE spacecraft [46] measured the CMB spectrum in the millimetre wavelength range, detecting an almost perfect black-body emission, the energy distribution of which is described by the Planck law:

$$I_\nu = \frac{2h\nu^3}{c^2}[exp(\frac{h\nu}{k_B T}) - 1]^{-1}. \tag{3.2}$$

The peak of this distribution was at $\lambda \approx 2$mm, which according to the Wien's displacement law, indicates a radiation temperature $T = 2.728 \pm 0.002\ K$. See Figure 3.3.

Following the theory developed so far, we expect the universe to be hotter and denser in the past, as it is constantly expanding and cooling. Since the energy density of a black body radiation is related to the temperature by the Stefan-Boltzmann law:

$$\rho_{rad} \propto T^4, \tag{3.3}$$

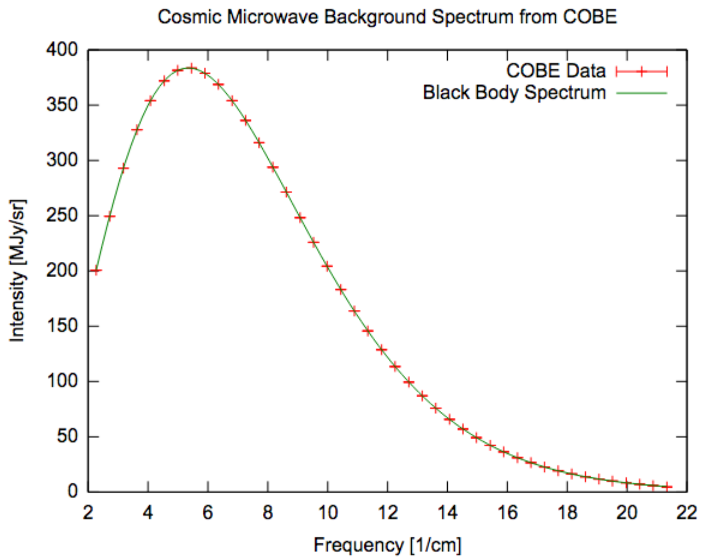

Figure 3.3: The CMB spectrum measured by the FIRAS instrument on the COBE, the most precisely measured black body spectrum in nature. The error bars are too small, and it is impossible to distinguish the observed data from the theoretical curve.

and we know from the continuity equation (2.10) that $\rho_{rad} \propto a^{-4}$, we get the following scaling of the temperature with redshift:

$$T(a) = \frac{1}{a}T(a_0),\ T(z) = (1+z)T(z=0). \tag{3.4}$$

The theory and observations of the CMB both support/confirm the existence of a primordial phase when ordinary matter in the universe was completely ionized due to the high temperature. The space was filled by hot plasma and compton-interaction coupled the photons and ions together strongly until the temperature dropped enough to allow the formation of hydrogen atoms (T $\sim$ 3000K). At this *recombination epoch* , the universe became nearly transparent to radiation because photons were no longer being scattered off of free electrons. Until the recombination epoch, the strong coupling between photons and matter established a condition of thermal equilibrium and thus the emission of a black body radiation. During its propagation toward the observer, the CMB radiation is affected by the cosmic expansion and the cosmological redshift induces a change of its temperature, according to Eq. (3.4). Another remarkable feature of the CMB radiation is its high isotropy. The angular distribution of the CMB temperature shows fluctuations on the order of 10^{-5}. These anisotropies can be statistically analyzed in order to constrain all cosmological parameters. The fundamental tool in this analysis is the angular power spectrum of the CMB. Analysis of the acoustic peaks in the angular power spectrum of the CMB, can constrain the curvature parameter: $\Omega_K \equiv 1 - \Omega_m - \Omega_{DE}$, and hence provide the strongest evidence for a spatially flat universe. The latest measures show that $\Omega_K h^2 = 0.1199 \pm 0.0027 \ll 1$ [37], however CMB data alone is not sufficient to distinguish between the contribution of matter and dark energy to the density of the universe. In Figure 3.1, the confidence regions for Ω_m and Ω_Λ are shown, as constrained by different cosmological observables. We see that an effective

way to break the degeneracy and to distinguish well between Ω_m and Ω_Λ, is to match the CMB data with other cosmological observables. In particular, the SN Ia show confidence contours perpendicular to those coming from CMB, hence helping constrain the parameters considerably.
The *Planck Surveryor* provides the state of the art data for CMB observations.

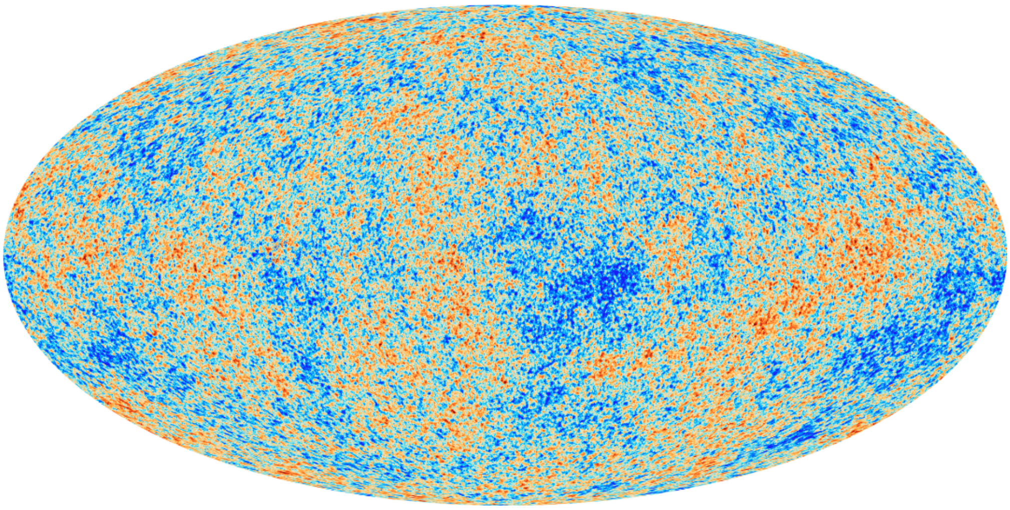

Figure 3.4: Cosmic Microwave Background as seen by Planck

Planck was a space observatory operated by the European Space Agency (ESA) from 2009 to 2013, consisting of a satellite orbiting around the second Lagrangian point of the Sun-Earth system. It mapped the full sky in 9 different channels from the radio to the sub-mm, providing excellent angular resolution (5 arcmin). The results for cosmological parameters as measured with Planck CMB data and other complementary observations, are provided below in Table 3.1.

Parameter	Planck 2013	Planck 2015
$\Omega_b h^2$	0.02205 ± 0.00028	0.02230 ± 0.00014
Ω_m	$0.315^{+0.018}_{-0.016}$	0.3089 ± 0.0062
Ω_Λ	$0.685^{+0.018}_{-0.016}$	0.6911 ± 0.0062
H_0	67.3 ± 1.2	67.74 ± 0.46
n_s	0.9603 ± 0.0073	0.9667 ± 0.0040
σ_8	0.829 ± 0.012	0.8159 ± 0.0086
z_*	1090.43 ± 0.54	1089.90 ± 0.23
Age/Gyr	13.817 ± 0.048	13.799 ± 0.23

Table 3.1: Cosmological parameter values for the ΛCDM model at 68% confidence limits. Column 2 give results from Planck temperature power spectrum data combined with Planck lensing data and WMAP polarization, see Table 2 of [37]. Column 3 combine the Planck temperature data with polarization, CMB lensing and other external data not collected by Planck, taken from Table 4 of [38]

3.3 Cosmological Constant

The cosmological constant Λ is most accepted candidate to explain the dynamics of our universe. It is a spatially uniform, time-independent component with an equation of state: $\omega = -1$. It was first introduced by Einstein as an additional contribution $\Lambda g_{\mu\nu}$ to his equation:

$$R_{\mu\nu} - \frac{1}{2} R g_{\mu\nu} + \Lambda g_{\mu\nu} = 8\pi G T_{\mu\nu}. \tag{3.5}$$

This represents the most general form of Einstein's field equations, consistent with the principle of general covariance. Thus, Λ can simply be interpreted as an additional freedom allowed by the theory of General Relativity. In addition, the cosmological constant can be also interpreted as a contribution to the stress-energy tensor coming from the vacuum energy, which is the energy associated with the ground state of quantum fields. Lorentz invariance requires that in any locally inertial reference frame, the energy-momentum tensor $T^{(vac)}_{\mu\nu}$ of the vacuum must be proportional to the Minkowski metric $\eta_{\mu\nu}$ (for which $\eta_{ij} = \delta_{ij}$, η_{00} = -1), hence in general reference frames $T^{(vac)}_{\mu\nu}$ must be proportional to $g_{\mu\nu}$.

$$T^{(vac)}_{\mu\nu} = -\rho_{vac} g_{\mu\nu} \Rightarrow p_{vac} = -\rho_{vac},\ \omega_{vac} = -1. \tag{3.6}$$

The equation of state for vacuum energy can be deduced by comparing the above stress-energy tensor with that of a perfect fluid Eq. (2.3). The identification between the vacuum energy and a cosmological constant contribution can be now obtained straightforwardly:

$$\Lambda g_{\mu\nu} = 8\pi G T^{(vac)}_{\mu\nu} \Rightarrow \rho_{vac} = \frac{\Lambda}{8\pi G} = \rho_\Lambda. \tag{3.7}$$

Inserting the FRLW metric in the extended Einstein equation (3.5), we obtain the following Friedmann equations:

$$\begin{aligned} H^2 \equiv & (\frac{\dot{a}}{a})^2 = \frac{8\pi G}{3}\rho - \frac{K}{a^2} + \frac{\Lambda}{3}, \\ \frac{\ddot{a}}{a} & = - \frac{4\pi G}{3}(\rho + 3p) + \frac{\Lambda}{3}. \end{aligned} \tag{3.8}$$

It is clear that the cosmological constant contributes negatively to the pressure term and hence exhibits a repulsive effect. The dynamics in the limit of pure Λ domination ($H^2 \approx \Lambda/3, \ddot{a}/a \approx \Lambda/3$) is given by the de-Sitter solution:

$$a(t) \propto exp(Ht), \tag{3.9}$$

$$H = \sqrt{\frac{\Lambda}{3}} = \sqrt{\frac{8\pi G \rho_\Lambda}{3}} = const. \tag{3.10}$$

3.4 Problems with Λ

From the Friedmann equations Eq. (3.8) and observation data, we know that Λ is of order of the present value of the Hubble parameter H_0:

$$\Lambda \approx {H_0}^2 \sim (10^{-42} GeV)^2 \Rightarrow \rho_\Lambda \sim 10^{-47} GeV^4. \tag{3.11}$$

This gives rise to a severe problem of fine tuning while addressing the problem from a quantum field theory point of view. Consider the contribution to the vacuum energy of a quantum field with mass m. In quantum field theory, each Fourier mode with wave vector k essentially behaves like an harmonic oscillator with frequency $\omega = \sqrt{k^2 + m^2}$ (we use natural units $c = \hbar = 1$) so that the contribution to the vacuum energy is a sum over all modes of the harmonic oscillator's zero point energy $E_0 = \frac{1}{2}\omega$:

$$\rho_{vac} = \frac{1}{4\pi^2} \int_0^\infty dk\ k^2 \sqrt{k^2 + m^2} \tag{3.12}$$

The energy density above exhibits an ultraviolet divergence: $\rho_{vac} \propto k^4$. However, we expect our current model of particle physics to be an effective theory, valid up to a cutoff scale E_c, in which case the integral (3.12) is finite. The Planck scale sets the limit at which GR and the Standard Model of quantum field theory are no longer reconcilable. Thus, assuming this cutoff to be the Planck energy $E_c = E_{Pl} \sim 10^{19}$, the integral (3.12) becomes:

$$\rho_{vac} = \frac{{E_{Pl}}^4}{16\pi^2} \sim 10^{74} GeV^4 \tag{3.13}$$

which is about 10^{121} orders of magnitude larger than the observed value given by Eq. (3.11). This popular discrepancy is called the *"cosmological constant problem"*. Since the procedure to "rescale" the zero point energy is ad hoc, one can try to properly cancel it by introducing counter terms. This requires an enormous fine-tuning to adjust ρ_Λ to the tiny, specific, observed value.
The problem can be slightly eased by assuming that the cutoff scale is lower than the Planck scale. For example, in supersymmetry (SUSY), the contributions to the vacuum energy of fermions and bosons exactly cancel each other out. If supersymmetry is indeed realized in nature, this means that we only have to integrate up to the scale of SUSY breaking $E_c = E_{SUSY}$. Taking $E_{SUSY} \sim 1\ TeV$, as is commonly expected, this would give $\rho_{vac} \sim 10^{12} GeV^4$, which still gives a discrepancy of 59 orders of magnitude. In order for the fine-tuning problem to disappear, one would need a cutoff scale of order $10^{-2} eV$. However, the standard model has been tested in accelerators up to energies in the TeV scale, so we truly cannot get around this huge fine-tuning problem.
Another theoretical problem arises from the fact that the observed values of $\Omega_m \approx 0.3$ and $\Omega_\Lambda \approx 0.7$ indicate that we are in a phase of transition from a pure matter dominated phase to a pure dark energy dominated phase. This is a very short phase by cosmological standards. In fact: $\frac{\rho_\Lambda}{\rho_m} \propto a^3$.
This problem of why the matter and dark energy densities should be of the same order exactly now, in the long history of our universe is called the *"coincidence problem"*.

3.5 Beyond Standard Model

The observations constrain the value of the equation of state of dark energy today, to be close to that of the cosmological constant $\omega_{DE} = -1.006 \pm 0.045$ [37]. Nevertheless, observations actually say relatively little about the time evolution of ω. We can consider a situation in which the equation of state of dark energy varies with time. Evolving scalar fields could mimic the action of a cosmological constant. This has not been ruled out by observations.

3.5.1 Dynamic dark energy

It is generally accepted that the universe has already experienced a phase of accelerated expansion known as "inflation" at its birth. Inflationary theories provide the correct initial conditions for the standard model of cosmology, solve the flatness and horizon problems as well, and explain the origin of density perturbations necessary for subsequent structure formation. Looking at inflationary theories, it is quite natural to consider that the accelerated expansion in the present epoch could also be driven by a scalar field. Scalar fields naturally arise in particle physics and can act as candidates for dark energy. So far, a wide variety of scalar-field dark energy models have been proposed. An extended review can be found in [39]. A typical example of such models are Quintessence theories, characterized by the action:

$$S = \int d^4x\sqrt{-g}[\frac{R}{16\pi G} - \frac{1}{2}g_{\mu\nu}\partial^\mu\phi\partial^\nu\phi - V(\phi)], \tag{3.14}$$

where g is the determinant of the metric tensor $g_{\mu\nu}$, and $V(\phi)$ is the potential of the field. The equation of motion of the scalar field in a flat FRLW space-time is obtained by varying the action with respect of ϕ:

$$\ddot{\phi} + 3H\dot{\phi} + \frac{dV}{d\phi}. \tag{3.15}$$

By varying the action with respect of the metric, we obtain the energy momentum tensor:

$$T_{\mu\nu} = \frac{-2}{\sqrt{-g}}\frac{\delta S}{\delta g} = \partial^\mu\phi\partial^\nu\phi - g_{\mu\nu}[g^{\alpha\beta}\partial_\alpha\phi\partial_\beta\phi + V(\phi)] \tag{3.16}$$

The scalar field is homogeneous and spatially independent at the background level: $\phi = \bar{\phi}(t)$, resulting in a substantially simplified energy momentum tensor:

$$\bar{T}_{\mu\nu} = \begin{pmatrix} -(\frac{1}{2}\dot{\phi}^2 + V(\phi)) & 0 \\ 0 & (\frac{1}{2}\dot{\phi}^2 - V(\phi))\delta_{ij} \end{pmatrix} \tag{3.17}$$

Note that at the background level, the scalar field behaves like a perfect fluid with:

$$\rho_\phi = (\frac{1}{2}\dot{\phi}^2 + V(\phi)),\ p_\phi = (\frac{1}{2}\dot{\phi}^2 - V(\phi)),\ \omega_\phi = \frac{\frac{1}{2}\dot{\phi}^2 - V(\phi)}{\frac{1}{2}\dot{\phi}^2 + V(\phi)}. \tag{3.18}$$

Inserting the above pressure and density above into the Friedmann equations, we get:

$$\begin{aligned} H^2 =& \frac{8\pi G}{3}[\frac{1}{2}\dot{\bar{\phi}}^2 + V(\bar{\phi})], \\ \frac{\ddot{a}}{a} =& -\frac{8\pi G}{3}[\dot{\bar{\phi}}^2 - V(\bar{\phi})] \end{aligned} \tag{3.19}$$

The last equation tells us that the scalar field produces an accelerated expansion and in fact, a nearly de-Sitter dynamics with $\omega_\phi \approx -1$ for: $\dot{\bar{\phi}}^2 \ll V(\bar{\phi})$. This condition is met when the potential is sufficiently flat to allow a slow-roll phase of the scalar field, thus producing a late-time inflationary phase. This is known as the "single field slow-roll scenario", and represents also the basic picture of primordial inflation. The slow roll condition allows us to get a rough estimate of the mass of the scalar field in quintessence models:

$$m_\phi = \sqrt{\frac{d^2 V_\phi}{d\phi^2}} \lesssim H_0 \sim 10^{-33} eV. \tag{3.20}$$

which is very small. The action in Eq. (3.14) shows that, in quintessence the scalar field is minimally coupled to gravity i.e., to the Einstein Hilbert term ($\sqrt{-g}\frac{R}{16\pi G}$), and it is not exactly coupled to matter. A coupling between scalar field and matter arises due to quantum corrections even if there isn't one at a classical level. Due to the expected small mass of the field, this coupling would produce long range forces that would be, in principle, observable. Unless there is an underlying symmetry suppressing these couplings, their values should be very small, in order to satisfy tests of gravity. This leads to another fine-tuning requirement in addition to the one necessary to make the cosmological constant small.

3.5.2 Modified Gravity

Modified gravity (MG) models are based on the idea of extending General Relativity through the addition of new degrees of freedom. They play an increasingly important role in cosmology as valid alternatives to ΛCDM model. There are two main reasons for investigating this idea from an observational and a theoretical point of view. Firstly, Einstein's GR has poorly been tested on scales larger than the solar system. This means that we hugely extrapolate the regime of GR's validity while using it in cosmological studies. Thus, it is important to understand the typical observational imprints allowing us to distinguish between alternative models of gravity on scales where GR has not yet been tested. Secondly, these kind of theories can explain the accelerated expansion of the universe without the need for the Λ term. This allows us to avoid the fine tuning problems. The idea is to assume that, for some unknown reason (e.g. some symmetry principle), the cosmological constant is exactly zero and the accelerated expansion is due to a modification of gravity that occurs on large scales. Our ignorance remains, but the problem now is easier to deal with.
In chapter 5, we discuss in detail the model of modified gravity used in this thesis, called the $f(R)$ models.

Chapter 4

SZ Effect & the Halo Model

Since we use the thermal Sunyaev Zel'dovich (tSZ) power spectrum in this thesis as a probe to test $f(R)$ modified gravity, we must first understand the SZ effect and the ingredients of the halo model used in the tSZ power spectrum computations:

4.1 The SZ Effect

In section 3.2 we discussed the cosmic microwave background radiation (CMBR). The SZ effect refers to a secondary distortion phenomenon of the CMBR through the process of inverse-compton scattering.

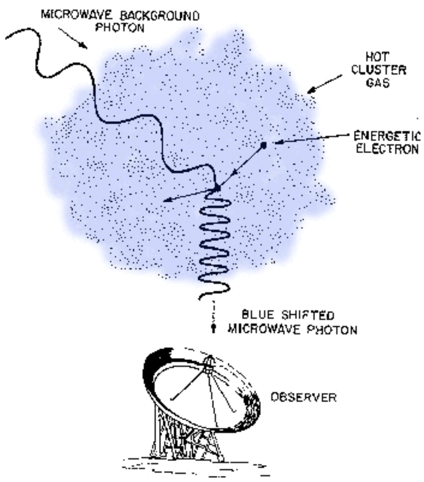

Figure 4.1: Schematic diagram of the SZ Effect.

Clusters of galaxies often have masses exceeding $3 \times 10^{14} M_{\odot}$, and gravitational radii, R, of megaparsecs order. About 9% of the mass of clusters of galaxies is in the form of distributed gas in the intra-cluster medium (ICM). The ICM is primarily composed of ordinary baryons, mostly ionized hydrogen and helium. If the gas in these clusters is in hydrostatic equilibrium, their electron temperature T_e can be given by:

$$k_B T_e \approx \frac{GMm_p}{2R} \approx 7(M/3 \times 10^{14} M_{\odot})(R/Mpc)^{-1} keV. \tag{4.1}$$

At such high temperatures, thermal emission from the ICM is in the X-ray, mainly by the bremsstrahlung process. These energetic electrons in the intra-cluster gas can scatter low-energy photons from the cosmic microwave background. The cross-section of these scatterings is given by the Thomson scattering cross-section, σ_T, giving us the optical depth $\tau_e \approx n_e \sigma_T R_{eff} \sim 10^{-2}$. The frequency of the photon is shifted slightly after the scattering, and on average there's a slight mean change in photon energy $(\Delta\nu/\nu) \approx (k_B T_e / m_e c^2) \sim 10^{-2}$. The overall change in brightness of the CMBR from inverse-compton (Thomson) scattering is therefore about 1 part in 10^4. This is about ten times larger than the cosmological signal in the CMB detected by COBE. Hence, this signal from the SZ effect is detectable, and can be distinguished by its spectral signature in the CMB spectrum. The amplitude of the SZ signal can also be correlated to other observables of galaxy clusters. The SZ effects have been studied for providing information on cluster structures, their dynamics, and on the Hubble flow by allowing methods for constraining cosmological parameters, like H_0. The special peculiarity of the SZ effect is that it is a redshift-independent phenomenon, making it easy to be observed up to high redshifts.

4.1.1 Inverse-Compton Scattering

When a photon is scattered by an electron, both the particles undergo a change in energy and direction of motion. The change in the photon is described by the usual Compton scattering formula [23]:

$$\epsilon' = \frac{\epsilon}{1 + \frac{\epsilon}{m_e c^2}(1 - cos\phi_{12})} \tag{4.2}$$

in the rest frame of the electron, where ϵ and ϵ' are the photon energies before and after the interaction, and ϕ_{12} is the angle by which the photon in deflected in the encounter (see Figure 4.2).

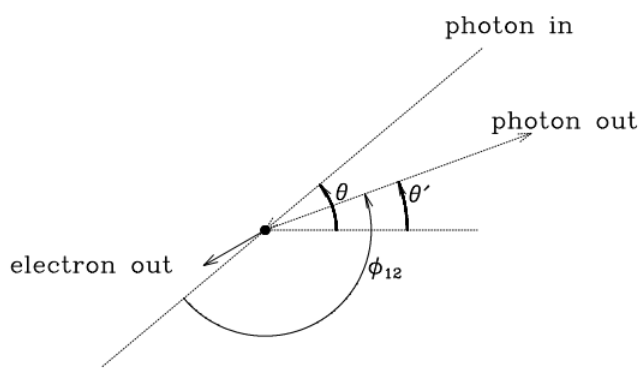

Figure 4.2: The scattering geometry, in the frame of rest of the electron before the interaction. An incoming photon, at angle θ is deflected by angle ϕ_{12}, and emerges after the scattering at angle θ'.

For low-energy photons and mild/non relativistic electrons, $\epsilon \ll m_e c^2$, the scattering is almost elastic ($\epsilon' = \epsilon$). This limit is appropriate for the scatterings in clusters that cause the SZ effect, and it simplifies the physics considerably. Here, inverse-compton scattering can be viewed as Thomson scattering in the rest frame of the electron, and the Thomson cross-section formula describes the interaction between a CMB photon and the electron. In this geometry, the probability of a scattering with angle θ is

$$p(\theta)d\theta = p(\mu)d\mu = (2\gamma^4(1-\beta\mu)^3)^{-1}d\mu \tag{4.3}$$

where the electron velocity $v_e = \beta c$, and $\mu = cos\theta$. The probability of a scattering to angle θ' is, [20][21]

$$\phi(\mu';\mu)d\mu' = (3/8)(1+\mu^2\mu'^2+\frac{1}{2}(1-\mu^2)(1+\mu^2))d\mu' \tag{4.4}$$

and the change of photon direction changes the scattered photon's frequency to:

$$\nu'' = \nu(1+\beta\mu')(1-\beta\mu)^{-1} \tag{4.5}$$

where $\mu' = cos\theta'$. By conventional, we define:

$$s = \log(\nu''/\nu) \tag{4.6}$$

which is the logarithmic frequency shift caused by a scattering. The probability that a single scattering of the photon causes a frequency shift s from an electron with speed βc is:

$$P(s;\beta)ds = \int p(\mu)d\mu\phi(\mu';\mu)(\frac{d\mu'}{ds})ds. \tag{4.7}$$

Using (Eq. 4.3-4.5), this becomes

$$P(s;\beta)ds = \frac{3}{16\gamma^4\beta}\int_{\mu_1}^{\mu_2}(1+\beta\mu')(1+\mu^2\mu'^2+\frac{1}{2}(1-\mu^2)(1+\mu^2))(1-\beta\mu')^{-3}d\mu \tag{4.8}$$

where μ' can be expressed in terms of μ and s as

$$\mu' = \frac{e^s(1-\beta\mu)-1}{\beta} \tag{4.9}$$

(from Eq. 4.5 and 4.6). The resulting function for several values of β is shown in Figure 4.3.

The increasing asymmetry of $P(s;\beta)$ as β increases is caused by relativistic beaming, and the width of the function to zero intensity in s,

$$\Delta s_0 = 2\log(\frac{1+\beta}{1-\beta}) \tag{4.10}$$

increases because increasing β causes the frequency shift related to a given photon angular deflection to increase.

The distribution of photon frequency shifts caused by scatterings by a population of electrons, rather than a single electron, is calculated from $P(s;\beta)$ by averaging over the electron β distribution. Thus, for photons that have been scattered once, the probability distribution of s, $P_1(s)$, is given by

$$P_1(s) = \int_{\beta_{lim}}^{1} p_e(\beta)d\beta P(s;\beta) \tag{4.11}$$

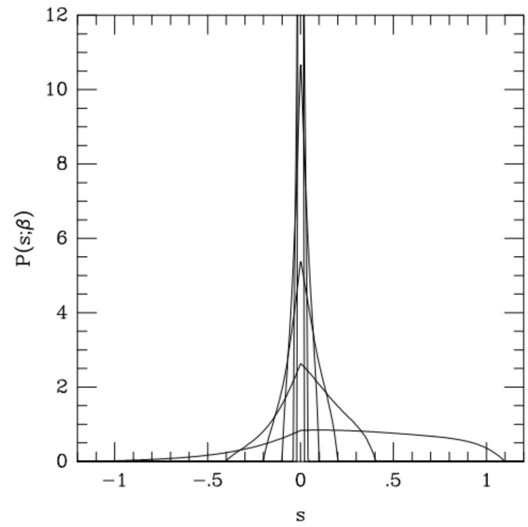

Figure 4.3: The scattering probability function $P(s;\beta)$, for $\beta = 0.01$, 0.02, 0.05, 0.10, 0.20, and 0.50. The function becomes increasingly asymmetric and broader as β increases

where β_{lim} is the minimum value of β capable of causing a frequency shift s,

$$\beta_{lim} = \frac{e^{|s|} - 1}{e^{|s|} + 1} \tag{4.12}$$

Note that, in deriving Eq. 4.8, it was assumed that the electron distribution $p_e(\beta)$ must not have such large Lorentz factors, γ, that our assumption of elastic scattering with the Thomson scattering cross-section is violated. For CMB photons, these assumptions are satisfied for $\gamma \lesssim 2 \times 10^9$. In clusters of galaxies the typical electron temperatures may be as much as 15 keV, but the corresponding Lorentz factors are still small, so we may ignore relativistic corrections to the scattering cross-section.

4.1.2 Spectrum Distortion

Let us use the result for the frequency shift in a single scattering to calculate the form of the scattered spectrum of the CMBR. The incident spectrum is given by:

$$I_0(\nu) = \frac{2h\nu^3}{c^2}[exp(\frac{h\nu}{k_B T}) - 1]^{-1}. \tag{4.13}$$

If every photon is scattered once, then the resulting spectrum becomes:

$$\frac{I(\nu)}{\nu} = \int_0^\infty d\nu_0 P_1(\nu, \nu_0) \frac{I_0(\nu_0)}{\nu_0}. \tag{4.14}$$

where $P_1(\nu, \nu_0)$ is the probability that a scattering occurs from frequency ν_0 to ν, and $I(\nu)/h\nu$ is the spectrum in photon number terms. Since $P_1(\nu, \nu_0) = P_1(s)/\nu$, where $P_1(s)$ is the frequency shift function in (4.11), this can be rewritten as a convolution in $s = \ln(\nu/\nu_0)$,

$$I(\nu) = \int_{-\infty}^{\infty} P_1(s) I_0(\nu_0) ds. \tag{4.15}$$

Consequently, the change in the radiation spectrum at frequency ν is:

$$\Delta I(\nu) = I(\nu) - I_0(\nu) = \frac{2h}{c^2}\int_{-\infty}^{\infty} P_1(s)ds(\frac{\nu_0^3}{e^{h\nu_0/k_BT}-1} - \frac{\nu^3}{e^{h\nu/k_BT}-1}) \quad (4.16)$$

The functions $\Delta I(\nu)$ shows a decrease in intensity at low frequency due to the shift of the Rayleigh-Jeans part of the spectrum to higher frequency resulting from the mean upward shift of the photon frequencies caused by scattering. Similarly, we see an intensity decrease in the Wien part of the spectrum: (see Figure 4.4 and 4.5)

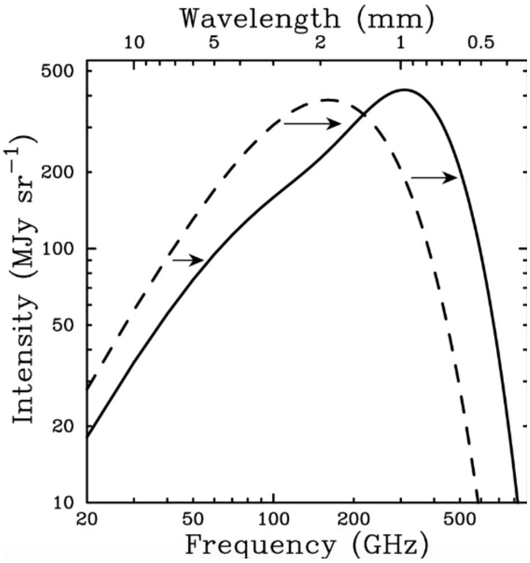

Figure 4.4: The Cosmic Microwave Background (CMB) spectrum, undistorted (dashed line) and distorted by the Sunyaev-Zel'dovich effect (SZE) (solid line), for a fictional cluster 1000 times more massive than a typical massive galaxy cluster. 218 GHz is the threshold frequency for the SZ effect shown above as the intersection point.

More generally, a photon entering the electron distribution may be scattered multiple times by electrons. If the optical depth to scattering through the electron cloud is τ_e, the resulting intensity change has the same form, but with an amplitude reduced by a factor τ_e. This is given explicitly as

$$\Delta I(\nu) = \frac{2h}{c^2}\tau_e\int_{-\infty}^{\infty} P_1(s)ds(\frac{\nu_0^3}{e^{h\nu_0/k_BT}-1} - \frac{\nu^3}{e^{h\nu/k_BT}-1}) \quad (4.17)$$

An important result already clear from (4.17) is that the intensity change caused by the SZ effect is redshift-independent, depending only on intrinsic properties of the scattering medium, making it a remarkable cosmological probe at a wide range of redshifts.

4.1.3 Thermal SZ effect

We saw above that passage of radiation through an electron population with significant energy content will produce a distortion of the radiation's spectrum.

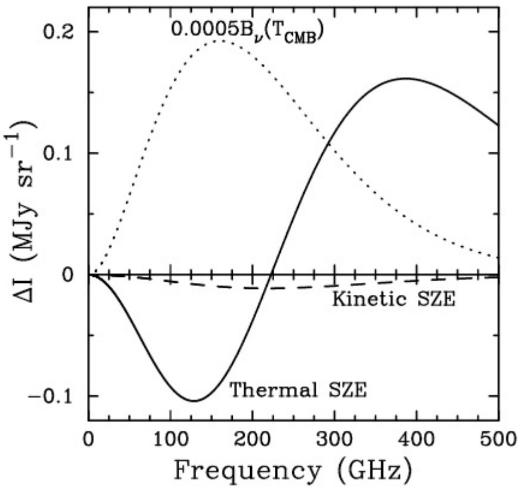

Figure 4.5: Intensity of the spectral distortion of the CMB due to the SZ effect, for an electron temperature of 10 keV, a Compton y parameter of 10^{-4}, and a peculiar velocity of 500 kms^{-1}. The thick solid line is the thermal SZE and the dashed line is the kinetic SZE. For reference, the 2.7 K thermal spectrum for the CMB intensity scaled by 0.0005 is shown by the dotted line.

If a cluster atmosphere contains gas with electron concentration $n_e(\mathbf{r})$, then the scattering optical depth, and the compton parameter along a particular line of sight are given as:

$$\tau_e = \int n_e(\mathbf{r})\sigma_T dl, \tag{4.18}$$

$$y = \int n_e(\mathbf{r})\sigma_T \frac{k_B T_e(\mathbf{r})}{m_e c^2} dl, \tag{4.19}$$

Most detailed information on the cluster structures is obtained from X-ray astronomy satellites. But, it is not possible to predict accurately the distribution of y on the sky from the X-ray surface brightness spectra.

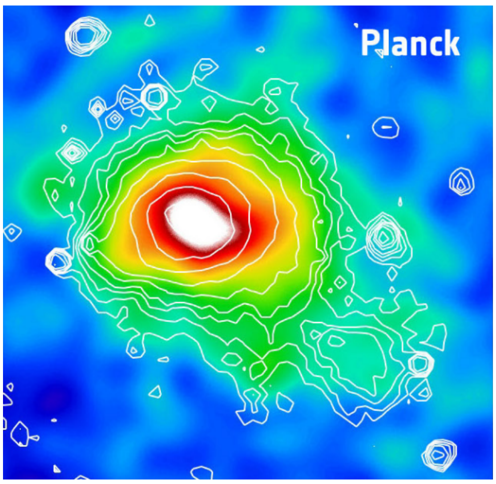

Figure 4.6: The gas of the Coma galaxy cluster as it appears in Planck through the Sunyaev-Zel'dovich effect (colors) and in X-rays (contour lines).

It is quite convenient to introduce a parameterized model for the properties of the cluster gas, and to fit the parameter values to the X-ray data. The integral (4.19) can then be performed to predict the appearance of the cluster in the SZ effect (Figure 4.6). A form that is convenient, simple, and popular is the isothermal β model, where it is assumed that the electron temperature T_e is constant and that the electron number density follows the spherical distribution

$$n_e(\mathbf{r}) = n_{e0}(1 + \frac{r^2}{r_c^2})^{-3\beta/2}. \tag{4.20}$$

Under these assumptions the cluster will produce circularly-symmetrical patterns of scattering optical depth, compton parameter with:

$$\tau_e(\theta) = \tau_{e0}(1 + \frac{\theta^2}{\theta_c^2})^{\frac{1}{2}-\frac{3}{2}\beta}, \tag{4.21}$$

$$y(\theta) = y_0(1 + \frac{\theta^2}{\theta_c^2})^{\frac{1}{2}-\frac{3}{2}\beta}, \tag{4.22}$$

where $\tau_{e0} = n_{e0}\sigma_T r_c\sqrt{\pi}\frac{\Gamma(\frac{3}{2}\beta-\frac{1}{2})}{\Gamma(\frac{3}{2}\beta)}$, and $y_0 = \tau_{e0}\frac{k_B T_e}{m_e c^2}$.
θ is the angle between the center of the cluster and the direction of interest and $\theta_c = r_c/D_A$ is the angular core radius of the cluster as deduced from the X-ray data. D_A is the angular diameter distance of the cluster.

4.2 The Halo Model

The halo model approach assumes that all the mass in the universe is partitioned into distinct units called halos that are small compared to the typical distances between them. This implies that the statistics of the mass density field on small scales are determined by the spatial distribution within the halos, therefore the way in which the halos are organized into large scale structures (LSS) is not important. On the other hand, the details of the internal structure of the halos isn't important on scales larger than a typical halo, therefore the only important element is the spatial distribution of the halos. Hence, the distribution of the mass in our universe can be studied in two steps: the distribution of mass within each halo, and the spatial distribution of the halos themselves. This approach is what makes up the halo model. This section describes the mass-dependent quantities that we can get from the halo model approach: like the abundance, spatial distribution, and internal pressure profiles of halos. In the subsections that follow, we will describe the models for these quantities that we use in this thesis to get the tSZ power spectrum.

4.2.1 Spherical Collapse Model

The spherical collapse model is a simple and useful approximation of formation of non-linear objects from a spherical collapse. The spherical collapse starts from an initially top-hat density perturbation of comoving size R_0. Let δ_i denote the initial density contrast within this region. Supposing that the initial fluctuations are gaussian with an rms value on scale R_0, we have $|\delta_i| \ll 1$. Hence, the mass contained in R_0 is $M_0 = (4\pi R_0^3/3)\bar{\rho}(1 + \delta_i) \approx (4\pi R_0^3/3)\bar{\rho}$ where $\bar{\rho}$ is the comoving background density. Let R denote the comoving size of this region at some later time, where the density contrast can be given by $(R_0/R)^3 \equiv (1+\delta)$. In the spherical collapse model, we get a deterministic relation between the initial comoving size R_0, the density of an object, and its Eulerian size R at a later time. The parametric solution for $R(z)$ for an Einstein-de Sitter (EdS) universe is:

$$\frac{R(z)}{R_0} = \frac{(1+z)}{(5/3)|\delta_0|}\frac{(1-\cos\theta)}{2}\ , \ \frac{1}{1+z} = (3/4)^{2/3}\frac{(\theta-\sin\theta)^{2/3}}{(5/3)|\delta_0|} \tag{4.23}$$

where δ_0 denotes the initial density contrast δ_i extrapolated to the present time using linear theory. In the spherical collapse model, initially overdense regions start to collapse at $\theta = 0$, and 'turnaround' at $\theta = \pi$, and have finished collapsing by $\theta = 2\pi$. From Eq. 4.23, we see that the size of an overdense region evolves as

$$\frac{R_0}{R(z)} = \frac{6^{2/3}}{2}\frac{(\theta-\sin\theta)^{2/3}}{(1-\cos\theta)}. \tag{4.24}$$

At turnaround, $\theta = \pi$, we get $[R_0/R(z_{ta})]^3 = (3\pi/4)^2$, hence the average density at the turnaround point is about 5.55 times that of the background universe, and is even higher at collapse: $R(z_{col}) = 0$, so the density at collapse is infinite. In fact, the region does not actually collapse to a vanishing point, but virializes at some non-zero size. To get the average density within the virialized object, let's assume that the region virializes at half the value of the turnaround physical radius, after the turnaround. Going from the turnaround to the collapse, the background universe would expand by a factor of $(1+z_{ta})/(1+z_{col}) = 2^{2/3}$ (from Eq 4.23), hence the virialized object is eight times denser than it was at turnaround (because $R_{vir} = R_{ta}/2$). The background density at turnaround is $(2^{2/3})^3 = 4$ times the background density at z_{vir}. Therefore, the virialized object is:

$$\Delta_{vir} \equiv (9\pi^2/16) \times 8 \times 4 = 18\pi^2, \tag{4.25}$$

times the density of the background at virialization. Additionally, the first equation of (4.23) shows that if the region is to collapse at z, the average density within it must have had a critical value, δ_{sc}, given by

$$\frac{\delta_{sc}(z)}{1+z} = \frac{3}{5}(3\pi/2)^{2/3} \tag{4.26}$$

Thus, in a collapsed region, the initial overdensity, extrapolated using linear theory to the time of collapse, is $\delta_{sc}(z)$. Eq. 4.25 says that the object is about 178 times denser than the background.

Note that, since $(1+\delta) = (R/R_0)^3$, the equations above provide a relation between the actual overdensity δ, and that predicted by linear theory, δ_0, and moreover, this relation is the same for all R_0. Because the mass of the object is proportional to R_0^3, the critical density for collapse δ_{sc} is mass-independent. This is an important and useful feature of the spherical collapse model. The parametric solution of (4.23) can be written as a formal series expansion, like below:

$$\frac{\delta_0}{1+z} = \sum_{k=0}^{\infty} a_k\delta^k = \delta - \frac{17}{21}\delta^2 + \frac{341}{567}\delta^3 - \frac{55805}{130977}\delta^4 + ... \tag{4.27}$$

At the lowest order, this is equivalent to the linear theory: δ is the initial δ_0 times the growth factor. A good approximation of the above expansion, which is also valid when $\delta \gg 1$, is:

$$\frac{\delta_0}{1+z} = \frac{3(12\pi)^{2/3}}{20} - \frac{1.35}{(1+\delta)^{2/3}} - \frac{1.12431}{(1+\delta)^{1/2}} - \frac{0.78785}{(1+\delta)^{0.58661}} \tag{4.28}$$

Note that the collapse is never spherical, and here we only showed an ad-hoc estimate of the virial density. Ellipsoidal collapses, for example, have different description of the $\delta_0(\delta)$ relation. In this thesis, we use an $f(R)$ modified spherical collapse model (discussed in chapter 5) to get the power spectrum results presented in chapter 6.

4.2.2 Halo Mass Function

Let us define the mass of a dark matter halo, $M_{\delta,c}(M_{\delta,d})$ as the mass enclosed within a sphere of radius $r_{\delta,c}(r_{\delta,d})$ such that the enclosed density is δ times the critical (mean matter) density at redshift z. The c subscripts refer to masses referenced to the critical density at redshift z, $\rho_{cr}(z) = 3H^2(z)/8\pi G$, whereas d subscripts refer to masses referenced to the mean matter density at redshift z, $\bar{\rho}_m(z) \equiv \bar{\rho}_m$ (constant in comoving units).
M is the virial mass enclosed within a radius:

$$r_{vir} = (\frac{3M}{4\pi\Delta_{cr}(z)\rho_{cr}(z)})^{1/3} \tag{4.29}$$

where $\Delta_{cr}(z) = 18\pi^2+82(\Omega(z)-1)-39(\Omega(z)-1)^2$ and $\Omega(z) = \Omega_m(1+z)^3/(\Omega_m(1+z)^3+\Omega_\Lambda)$. Often it's convenient to convert between M and various other spherical-overdensity masses (e.g., M_{200c} or M_{200d}), which can be done using the NFW density profile [18] and the concentration-mass relation from [19]. For this, we have to solve the following non-linear equation for $r_{\delta,c}$ (or $r_{\delta,d}$):

$$\int_0^{r_{\delta,c}} 4\pi r'^2 \rho_{NFW}(r', M, c_{vir}) dr' = (4/3)\pi r_{\delta,c}^3 \rho_{cr}(z)\delta \tag{4.30}$$

where $c_{vir} \equiv r_{vir}/r_{NFW}$ is the concentration parameter (r_{NFW} is the NFW scale radius). After solving Eq. 4.3 to find $r_{\delta,c}$, we can calculate $M_{\delta,c}$ using $M_{\delta,c} = (4/3)\pi r_{\delta,c}^3 \rho_{cr}(z)\delta$.
The halo mass function, $dn(M,z)/dM$ describes the comoving number density of halos per unit mass as a function of redshift. We follow the approach developed by Press and Schechter [11] and refined by others:

$$\begin{aligned}\frac{dn(M,z)}{dM} =& \frac{\bar{\rho}_m}{M} \frac{d\ \ln(\sigma^{-1}(M,z))}{dM} f(\sigma(M,z)) \\ =& -\frac{\bar{\rho}_m}{2M^2} \frac{R(M)}{3\sigma^2(M,z)} \frac{d\sigma^2(M,z)}{dR(M)} f(\sigma(M,z)),\end{aligned} \tag{4.31}$$

where $f(\sigma(M,z))$ is known as the halo multiplicity function, $\sigma^2(M,z)$ is the variance of the linear matter density field smoothed with a (real space) top-hat filter on a scale $R(M) = (\frac{3M}{4\pi\bar{\rho}_m})^{1/3}$ at redshift z, and given by:

$$\sigma^2(M,z) = \frac{1}{2\pi^2} \int k^3 P_{lin}(k,z) W^2(k, R(M)) d\ln k, \tag{4.32}$$

where $P_{lin}(k, z)$ is the linear theory matter power spectrum at wavenumber k and redshift z. $W(k, R)$ is called the *window function*, which here is a top-hat filter in real space, and is given in Fourier space by:

$$W(k, R) = \frac{3}{x^2}(\frac{\sin x}{x} - \cos x), \tag{4.33}$$

where $x \equiv kR$. To calculate the tSZ power spectrum in ΛCDM gravity, we use the parametrization and calibration from [12], where computations are performed in terms of the spherical-overdensity masses with respect to the mean matter density, $M_{\delta,d}$, for a variety of overdensities. The halo multiplicity function in this model is parametrized by

$$f(\sigma(M, z)) = A[(\frac{\sigma}{b})^{-a} + 1]e^{-c/\sigma^2} \tag{4.34}$$

where $\{A,\ a,\ b,\ c\}$ are fixed fit parameters from simulations. We use the values of these parameters appropriate for the $M_{200,d}$ halo mass function from [12] with the redshift-dependent parameters given in their Eq. (5)-(8). From now on, we refer to this as the *Tinker mass function*, which we use in our power spectrum calculations.

4.2.3 Bias

Dark matter halos are biased tracers since they cluster more strongly than the underlying matter density field. This bias can depend on scale, mass, and redshift. The halo bias $b(k, M, z)$ can be defined as:

$$b(k, M, z) = \sqrt{\frac{P_{hh}(k, M, z)}{P(k, z)}}, \tag{4.35}$$

where $P_{hh}(k, M, z)$ is the power spectrum of the halo density field and $P(k, z)$ is the power spectrum of the matter density field. The halo bias is a necessary factor in modeling the cosmological information we get from galaxy clusters. We will need it to compute the two-halo term of the tSZ power spectrum, which requires knowledge of $P_{hh}(k, M, z)$.

In this thesis, we use the fitting function in Eq. 6 of [26] to compute this linear Gaussian bias, $b_G(M, z)$, with the parameters appropriate for $M_{200,d}$ (Table 2 in [26]). This fit was determined from the results of many large-volume N-body simulations with a variety of cosmological parameters and found to be quite accurate. We will refer to this prescription as the *Tinker bias model.*

The modification of halo bias in modified gravity is beyond the scope of this thesis, so we will be using the same bias to calculate the tSZ power spectrum in both the ΛCDM and $f(R)$ gravity scenarios.

4.2.4 Halo Profile

This thesis uses the parametrized ICM pressure profile fit from [29] as our fiducial model, derived from the cosmological hydrodynamics simulations in [30]. The ICM thermal pressure profile in this model is parametrized as below:

$$\frac{P_{th}(x)}{P_{200,c}} = \frac{P_0(x/x_c)^\gamma}{[1 + (x/x_c)^\alpha]^\beta}\ ,\ x \equiv r/r_{200,c}, \tag{4.36}$$

where the thermal pressure profile, $P_{th}(x) = 1.932 P_e(x)$, x is the dimensionless distance from the cluster center, x_c is a core scale length, P_0 is a dimensionless amplitude, α, β , and γ describe the logarithmic slope of the profile at intermediate ($x \sim x_c$), large ($x \gg x_c$), and small ($x \ll x_c$) radii, respectively, and $P_{200,c}$ is the self-similar amplitude for pressure at $r_{200,c}$ given by:

$$P_{200,c} = \frac{200 G M_{200,c} \rho_{cr}(z) \Omega_b}{2 \Omega_m r_{200,c}} \tag{4.37}$$

In [30], this parametrization is fit to the stacked pressure profiles of clusters extracted from the simulations. The mass and redshift dependence of these parameters captures deviations from simple self-similar cluster pressure profiles. These deviations arise from non-gravitational energy injections due to AGN and supernova feedback, star formation in the ICM, and non-thermal processes such as turbulence and bulk motions. The equations above completely specify the ICM electron pressure profile as a function of mass and redshift, which in addition to the halo mass function and halo bias, provides the remaining part needed for the tSZ power spectrum calculations in this thesis. We will refer to this model of the ICM pressure profile as the *Battaglia profile.* The Battaglia pressure profile has been verified to be in good agreement with a number of observations of cluster pressure profiles.

Just like the halo bias, we also keep the pressure profile the same even in the $f(R)$ gravity scenario, as modifications of the profile in alternative gravities is beyond the scope of this thesis.

4.3 tSZ Power Spectrum

Note that the tSZ power spectrum calculations here are done in terms of the virial mass M, but we can always compute $dM_{200,d}/dM$ using Eq. 4.30 in order to convert the Tinker mass function $dn/dM_{200,d}$ to a virial mass function $\frac{dn}{dM} = \frac{dn}{dM_{200,d}} \frac{dM_{200,d}}{dM}$ for our analysis.

The temperature shift caused by the tSZ effect, ΔT at angular position $\vec{\theta}$ with respect to the center of a cluster of mass M at redshift z is given by

$$\begin{aligned} \frac{\Delta T(\vec{\theta}, M, z)}{T_{CMB}} &= g_\nu y(\vec{\theta}, M, z) \\ &= g_\nu \frac{\sigma_T}{m_e c^2} \int_{LOS} P_e\left(\sqrt{l^2 + d_A^2 |\vec{\theta}|^2}, M, z\right) \, dl \ , \end{aligned} \tag{4.38}$$

where $g_\nu = x \coth(x/2) - 4$ is the tSZ spectral function with $x \equiv h\nu / k_B T_{CMB}$, y is the Compton-y parameter, σ_T is the Thomson scattering cross-section, m_e is the electron mass, and $P_e(\vec{r})$ is the ICM electron pressure at location $\vec{r}$ with respect to the cluster center.

We have neglected relativistic corrections, as these effects are relevant only for the most massive clusters in the universe ($\gtrsim 10^{15}\ M_\odot/h$). Such clusters contribute non-negligibly to the tSZ power spectrum at low-l, and thus our results in unmasked calculations may be slightly inaccurate. But relativistic corrections are very difficult to be made and goes beyond the scope of this thesis.

All of our calculations in this thesis are phrased in a frequency-independent manner in terms of the Compton-y parameter, and we will often use "y" as a label for tSZ quantities.

We compute the tSZ power spectrum using the halo model approach discussed above. Complete derivations of all the relevant expressions is given in Appendix A of [32], first obtaining completely general full-sky results and then using the flat-sky/Limber approximation [22]. Here, we simply quote the necessary results. The tSZ power spectrum, C_l^y, is given by the sum of the one-halo and two-halo terms: $C_l^y = C_l^{y,1h} + C_l^{y,2h}$.

In the flat-sky limit, the one-halo term simplifies to the following widely-used expression (Eq. 1 of [25]):

$$C_l^{y,1h} \approx \int dz \frac{d^2V}{dzd\Omega} \int dM \frac{dn(M,z)}{dM} |\tilde{y}_l(M,z)|^2, \tag{4.39}$$

where,

$$\tilde{y}_l(M,z) \approx \frac{4\pi r_s}{l_s^2} \int dx\ x^2 \frac{\sin((l+1/2)x/l_s)}{(l+1/2)x/l_s} y_{3D}(x;M,z) \tag{4.40}$$

Here, r_s is a characteristic scale radius (not the NFW scale radius) of the y_{3D} profile given by $y_{3D}(\vec{r}) = \frac{\sigma_T}{m_e c^2} P_e(\vec{r})$ and $l_s = a(z)\chi(z)/r_s = d_A(z)/r_s$ is the multipole moment associated with the scale radius. For the Battaglia pressure profile used in our calculations, the natural scale radius is $r_{200,c}$. In our calculations, we choose to implement the flat-sky result for the one-halo term at all l.
In the Limber approximation, the two-halo term simplifies to:

$$C_l^{y,2h} \approx \int dz \frac{d^2V}{dzd\Omega} P_m(k) D_+^2(z) [\int dM \frac{dn(M,z)}{dM} b(k,M,z) |\tilde{y}_(M,z)]^2 \tag{4.41}$$

where $P_m(k)$ is the linear matter power spectrum, $k = (l+1/2)/\chi(z)$, $D_+(z)$ is the growth factor, and $d^2V/dzd\Omega = c\chi^2(z)/H(z)$ is the comoving volume element per steradians.

We use the halo mass functions, and the bias models, and the ICM electron pressure profile in Eq. (4.39) and (4.41). This approach to calculate the tSZ power spectrum separates the cosmology-dependent quantities, the mass function and bias, from the ICM-dependent component, the pressure profile. This is because the small-scale baryonic physics that determines the structure of the ICM pressure profile doesn't participate in the large-scale physics described by the background cosmology and linear perturbation theory.
Also note that because the tSZ signal is heavily dominated by contributions from collapsed objects, the halo model approximation gives very accurate results. Particularly, the halo model agrees very well with the simulation results for $l \lesssim 1000$, which is the regime we are interested in for this thesis. On smaller angular scales, effects due to asphericity and substructure become important, which are not captured in the halo model approach. We don't expect the contributions from the intergalactic medium, and other diffuse structures to significantly impact the calculations and forecasts in this thesis.

Chapter 5

Modified Gravity

When Mercury's perihelion precession was discovered, a French mathematician, Urbain Le Verrier, ascribed this anomaly to the existence of a hypothetical planet called Vulcan between the Sun and Mercury. As we now know, we never found Vulcan and in fact, Newton's theory of gravity needed a revision by Einstein's general theory of relativity in order to explain this phenomenon. This story from the past is a good lesson to be open-minded when we encounter unexpected observations.
We need to consider all our assumptions made in the standard model of cosmology leading us to the cosmological constant problem. A big one is our full faith in Einstein's general relativity to explain gravity on all scales, when in fact, it has only been tested in our local universe. GR has been tested to satisfy in the Solar System and also been tested by binary pulsars. In the low curvature regimes, however, it has especially not been well tested. In such regimes, the standard model of cosmology requires dark energy to account for the universe's accelerating expansion. Since not much has been observed in favor of dark energy, here we have an opportunity to test gravity by means of cosmology.
Modified gravity has the potential to provide an interesting solution to the cosmological constant problem. Several theories of modified gravity have been proposed over the years. The 6-D *braneworld model* puts forwards the idea of modifying the way in which gravity responds to the cosmological constant. Some modified gravity models also pitch the idea of adding a small mass to the graviton, in order to explain the late time acceleration of the universe. 5-D *braneworld model* proposes another interesting idea of *self-acceleration*, where the universe can acceleratingly expand without the need of the cosmological constant. Unfortunately, we do not yet have a consistent model realizing these new ideas, but this should not stop us to challenge GR on cosmological scales.

Modifying general relativity is no easy task, however. Lovelock's theorem states that Einstein's equations are the only second-order local equations of motion for a metric derivable from the action in 4D. As such, if we modify GR, we are bound to end up with one or more of these:

- Extra degrees of freedom
- Higher derivatives
- Higher dimensional spacetime

- Non-locality

With these additional elements introduced into the theory, we need a consistency check of our theoretical model. The solutions have to be stable. Let's start with a simple scalar field action to discuss the several kinds of instabilities:

$$S = \int dtd^3x(K_t\dot{\phi}^2 - K_x(\partial_i\phi)(\partial^i\phi) - m^2\phi^2). \tag{5.1}$$

where ϕ is the scalar field. The tachyonic instability refers to the case when the scalar field has a negative mass squared i.e. $m^2 < 0$. If the instability time scale $|m|^{-1}$ is long enough, this instability can be ignored. When the gradient term $K_x < 0$, a more severe instability arises shortening the time scale on small scales. An even more severe instability is the ghost instability which arises when the kinetic term $K_t < 0$. In addition, the vacuum decays instantaneously at the quantum level, and hence is unstable. This can be avoided by introducing a non-Lorentz-invariant cut-off. Another common problem is known as the strong coupling problem where, in addition to the kinetic term, the scalar field has non-linear interaction terms. For example,

$$S_{non-linear} = \int d^4x\Lambda_3^3\Box\phi(\partial\phi)^2. \tag{5.2}$$

This non-linear interaction becomes important at energy scale higher than Λ_3 and in general, we loose control of the theory beyond Λ_3. This strong coupling scale is often associated with the energy scale related to the accelerated expansion of the universe, H_0, which is extremely small compared with the scale of gravity M_{Pl}. Thus, the strong coupling scale is often quite low in modified gravity models. Therefore, we should treat these theories as an effective theory, valid only at energy scales lower than Λ_3. Apart from theoretical consistency checks, modified gravity models also need to satisfy observational tests, like the well-established Solar System constraints. The deflection angle θ of stars due to the Sun is observed to be $\theta = (0.99992 \pm 0.00023) \times 1.75''$, where 1.75" is the prediction of GR. Another relativistic effect is time delay due to the effect of the Sun's gravitational field, which was measured very accurately by the Cassini satellite to be: $\Delta t = (1.00001 \pm 0.00001)\Delta t_{GR}$. Any modified theory of gravity needs to satisfy these Solar System constraints on deviations from GR in the. Also, the expansion of the universe should look very similar to that of the ΛCDM model in the background. Modified gravity models need to pass all these observational tests, and thus, it's no easy task constructing theories to modify GR.

5.1 $f(R)$ Models

First proposed in 1970 by Hans Adolph Buchdahl, $f(R)$ modified gravity is a generalization of Einstein's general relativity. It is a family of theories, where each one is defined by a different function f of the Ricci scalar R. The simplest case is just the function being equal to the scalar ($f(R) = R$), which is just the general relativity case. Introducing an arbitrary function can grant us some freedom to explain the accelerated expansion and structure formation without the need of dark energy or dark matter. These models have the prospect of producing a wide range of phenomena by adopting different functions.

In $f(R)$ gravity, the Einstein-Hilbert action is generalized to be a function of the Ricci curvature

$$S = \int d^4x\sqrt{-g}f(R) + \int d^4x\sqrt{-g}\mathcal{L}_m. \tag{5.3}$$

Being a fourth order equation of motion for the metric, it can be classified as a higher derivative theory. But, we can make the equation of motion second order by introducing a scalar field. The action becomes:

$$S = \int d^4x\sqrt{-g}(f(\phi) + (R-\phi)f'(\phi)). \tag{5.4}$$

Varying with respect to ϕ, we get $(R-\phi)f''(\phi) = 0$. We recover the original action if $f''(\phi) \neq 0$, and $R = \phi$. By defining $\psi = f'(\phi)$ and $V = f(\phi) - \phi f'(\phi)$, the action becomes:

$$S = \int d^4x\sqrt{-g}(\psi R - V(\psi)) \tag{5.5}$$

Here, if we ignore the potential, this model gets excluded by the Solar System constraints. But if we choose the potential i.e., the form of the $f(R)$ function appropriately, we incorporate a screening mechanism known as the *chameleon mechanism* to evade the Solar System constraint as we will see in the next sections. In general, the scalar tensor theory is described by the following action:

$$S = \int d^4x\sqrt{-g}(\psi R - \frac{\omega_{BD}(\psi)}{\psi}(\partial\psi)^2 - V(\psi) + \int d^4x\sqrt{-g}\mathcal{L}_m(g_{\mu\nu}). \tag{5.6}$$

where ω_{BD} is the Brans-Dicke parameter. To transform the action to the Einstein frame, we need a conformal transformation $g_{\mu\nu} = A(\phi)^2\bar{g}_{\mu\nu}$ and a redefinition of the scalar field:

$$S = \int d^4x\sqrt{-\bar{g}}(R - \frac{1}{2}(\partial\phi)^2 - \bar{V}(\phi) + \int d^4x\sqrt{-g}\mathcal{L}_m(A(\phi)^2\bar{g}_{\mu\nu}). \tag{5.7}$$

In this frame, the scalar field is directly coupled to matter. Many $f(R)$ models can be generated by choosing different function $f(R)$, but the successful models for the late time cosmology share some common features.

5.2 Chameleon Screening

Einstein's general relativity has been tested to high accuracy in the Solar System. Hence, any proposed modified gravity model needs to be able to satisfy GR on this scale, while explaining the accelerated expansion of the universe. There are two ways one can achieve that:

- One possibility is to break the equivalence principle. The Solar System constraints are obtained using objects made of baryons. So, if the additional degree of freedom only couples to dark matter, and not to baryons, it's possible to avoid these constraints while leaving us the possibility to modify gravity significantly on cosmological scales. These models where the scalar field is coupled only to dark matter is known as interacting dark energy models in the Einstein frame.

- If we want to keep the equivalence principle, we must provide a mechanism that suppresses (or "screens") the modification of gravity on small scales. The screening mechanism rests on the fact that the additional degree of freedom, represented by a scalar field, obeys a non-linear equation driven by the density, which varies over many orders of magnitude in our universe. The critical density of the universe $\rho_{crit} = 10^{-29} gcm^{-3}$, typical density inside galaxies $\rho_{gal} \simeq 10^{-24} gcm^{-3}$, and the density in the Sun $\rho_{sun} = 10 gcm^{-3}$. This implies a non-linear density contrast which instills a non-linearity in the scalar field, thus changing its behavior on different scales from the solar system to cosmological scales.

A general Lagrangian for a scalar field can be written as:

$$\mathcal{L} = -\frac{1}{2} Z^{\mu\nu}(\phi, \partial\phi, \partial^2\phi)\partial_\mu\phi\partial_\nu\phi - V(\phi) + \beta(\phi)T^\mu_\mu, \tag{5.8}$$

where $Z^{\mu\nu}$ is the derivative self-interactions of the scalar field, $V(\phi)$ is a potential, $\beta(\phi)$ is a coupling function and T^μ_μ is the trace of the matter energy-momentum tensor. In the presence of non-relativistic matter $T^\mu_\mu = -\rho$, the scalar field's dynamics depends on the local density of the system. Let the background field $\bar{\phi}$ depend on the local density. Around this background, the scalar field's dynamics is determined by three parameters: the mass $m(\bar{\phi})$, the coupling $\beta(\bar{\phi})$ and the kinetic function $Z^{\mu\nu}(\bar{\phi})$. These three parameters let us generate different types of "screening".

In [15], they present a scenario where scalar fields can evolve cosmologically while having couplings to matter of order unity, i.e., $\beta_i \sim \mathcal{O}(1)$. This is because the magnitude of scalar field mass depends on the local matter density. In high density regions, such as on Earth, the mass of the fields is large, exponentially suppressing the resulting violations of the equivalence principle. For large mass of fluctuations $m^2(\bar{\phi})$ in dense environments, the scalar field does not propagate above the Compton wavelength $m(\bar{\phi})^{-1}$ and hence the the scalar field force is suppressed.

Finally, on cosmological scales, where the density is very low, the mass can be of the order of the present Hubble parameter, small enough to allow the scalar field to generate a fifth force significantly modifying gravity, and thereby making it a potential candidate for causing the late-time acceleration of the universe. This is known as the *chameleon* type screening mechanism, which replies on the scalar fields to couple directly to baryons with gravitational strength. Models of this class can be represented by an action (5.7) in the Einstein frame:

$$S = \int d^4x\sqrt{-g}[\frac{R}{16\pi G} - \frac{1}{2}(\nabla\phi)^2 - V(\phi)] + S_m(A^2(\phi)g_{\mu\nu}). \tag{5.9}$$

The matter fields couple to a metric $A^2(\phi)g_{\mu\nu}$. This coupling allows a test particle to feel the fifth force $\nabla \ln A(\phi)$ generated by the scalar field. The dynamics of the scalar field in these models is determined by the effective potential which depends on the local density, and is given by:

$$V_{eff} = V(\phi) - [A(\phi) - 1]T^\mu_\mu. \tag{5.10}$$

The mass of the scalar field around the minimum of the potential $\phi = \bar{\phi}$ and the coupling function determine the dynamics of the scalar field:

$$m^2 = V''_{eff}(\bar{\phi}),\ \beta = M_{Pl}\frac{d\ln A}{d\phi}|_{\phi=\bar{\phi}} \tag{5.11}$$

The chameleon screening mechanism, discussed here, appoints the potential and the coupling function below:

$$A(\phi) = 1 + \xi \frac{\phi}{M_{Pl}},\ V(\phi) = \frac{M^{4+n}}{\phi^n}. \tag{5.12}$$

where the mass scale M is a model parameter. The mass m^2 in regions of high densities become large enough to suppress the force mediated by the scalar field. Since $A(\phi)$ is linear in ϕ, the second derivative of the effective potential does not depend on the energy density. In fact, the density dependence of the mass lies in the minimum of the potential $\bar{\phi}$.

This density-dependent mass for ϕ generates from the interplay of two source

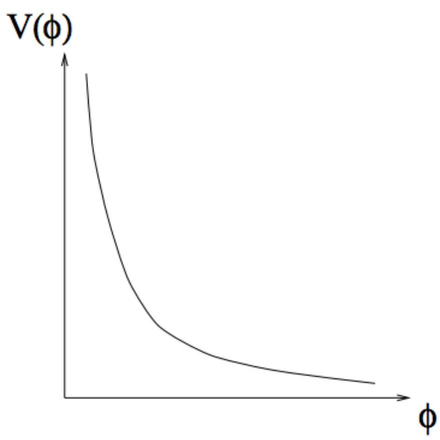

Figure 5.1: Example of a runaway potential.

terms in the equations of motion. The first is described by a monotonically-decreasing potential $V(\phi)$ of a runaway form (Figure 5.1), which accounts for self-interactions. And, the second term comes from the coupling between the scalar and matter fields, which is of the form $e^{\beta_i \phi / M_{Pl}}$.

The coupling constants β_i are allowed to have values of order unity or greater.

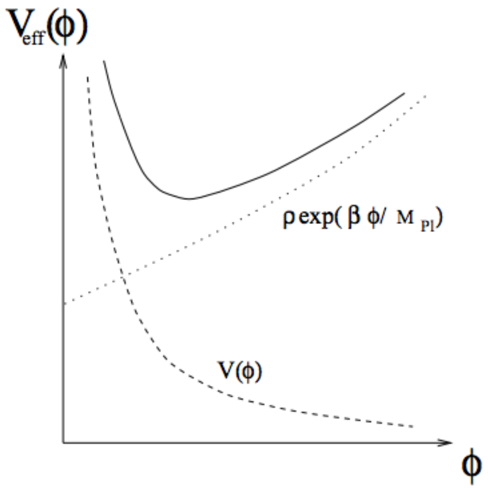

Figure 5.2: The chameleon effective potential V_{eff} (solid curve) is the sum of two contributions: one from the actual potential $V(\phi)$ (dashed curve), and the other from its coupling to the matter density ρ (dotted curve).

Although both of these are monotonic functions of ϕ, their combined effect results in an effective potential that exhibits a minimum (Figure 5.2). Furthermore, since this effective potential V_{eff} depends on the local matter density ρ, both the field value at the minimum and the mass of small fluctuations depend on ρ as well, with the latter being an increasing function of the density (Figure 5.3). Consequently, the chameleon screening is a direct consequence of the fact that scalar fields in these model have completely different behaviors in regions of high versus low densities.

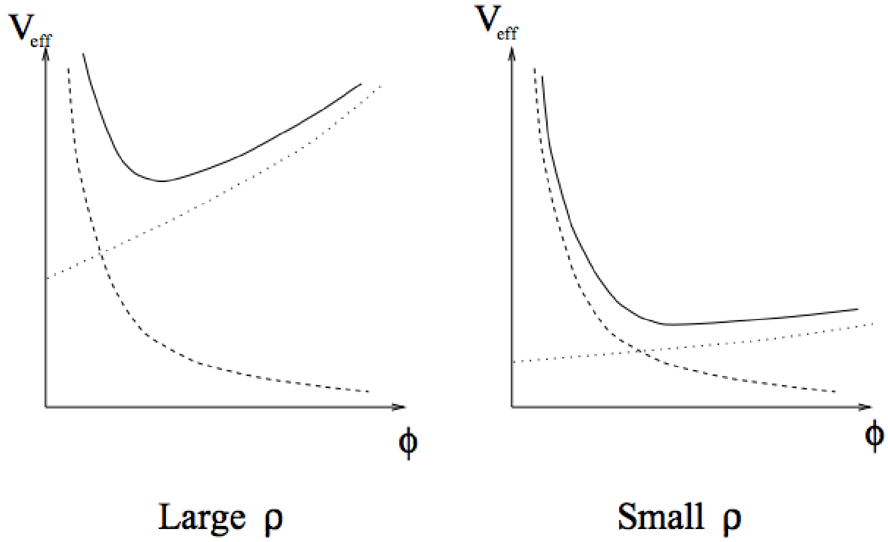

Figure 5.3: Chameleon effective potential for large and small ρ, respectively. This illustrates that, as ρ decreases, the minimum shifts to larger values of ϕ and the mass of small fluctuations decreases. (Line styles are the same as in Figure 5.2.)

ϕ is known as a "chameleon" field because of its physical properties (such as its mass) being sensitive to the environment. Moreover, in regions of high density, the chameleon can blend with its environment and become almost invisible to searches for equivalence principle violation and fifth force. As such, the chameleon models can satisfy all existing solar system constraints. This relies on the fact that the chameleon-mediated force between two large objects, such as the Earth and the Sun, is much weaker than one would guess.

We can think of the Earth as a collection of infinitesimal volume elements and

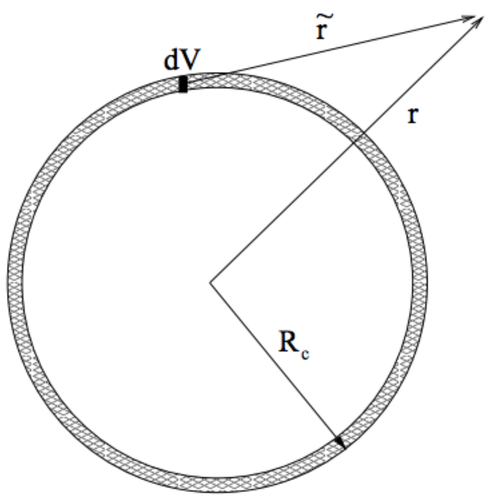

Figure 5.4: For large objects, the ϕ-field a distance $r > R_c$ from the center is to a good approximation entirely determined by the contribution from infinitesimal volume elements dV (dark rectangle) lying within a thin shell of thickness ΔR_c (shaded region). This thin-shell effect suppresses the resulting chameleon force

consider one such volume element located well-within the Earth. Since the mass of the chameleon is very large inside the Earth, the ϕ-flux from this volume element is exponentially suppressed and therefore contributes negligibly to the ϕ-field outside the Earth. This is true for all volume elements within the Earth, except for those located in a thin shell near the surface. Infinitesimal elements within this shell are so close to the surface that they do not suffer from the bulk exponential suppression (Figure 5.4). Thus, the exterior field is generated almost entirely by this thin shell. A similar argument can be made for the Sun. This is how the chameleon-mediated force between the Earth and the Sun is suppressed by this *thin-shell effect*, thereby ensuring that solar system tests of gravity are satisfied.

5.3 Hu-Sawicki Parametrization

As we already discussed, the fundamental issue is that $f(R)$ gravity introduces a scalar degree of freedom with the same coupling to matter as gravity, which is very small at the background low cosmological density. This extra degree of freedom produces a long-range fifth force, which would change the metric around the Sun to defy observations. Hence, we would want any proposed $f(R)$ model to simultaneously satisfy the solar-system constraints on deviations from general relativity as well as account for the late-time acceleration of the expansion of our universe.
Hu-Sawicki parametrization introduces a class of $f(R)$ models that are designed to meet these requirements:

- The cosmology should mimic ΛCDM in the high-redshift regime where it is well-tested by the CMB,
- It should accelerate the expansion at low redshift with an expansion history that is close to ΛCDM, but without a true cosmological constant,
- It should have sufficient degrees of freedom to encompass the currently accepted low-redshift observations,
- it should include the phenomenology of ΛCDM as a limiting case

Because of these qualities, it is a popular $f(R)$ model that has been used in several works ever since, including the papers on modeling the halo mass functions (HMF) in $f(R)$ gravity, used in this thesis. We discuss the HMF models in the next section.

Hu-Sawicki consider a modification to the Einstein-Hilbert action in the Jordan frame of the form:

$$S = \int d^4x\sqrt{-g}[\frac{R + f(R)}{2\kappa^2} + \mathcal{L}_m], \tag{5.13}$$

where R is the Ricci scalar, $\kappa^2 = 8\pi G$, and $\mathcal{L}_m$ is the matter Lagrangian.

The design of these models to satisfy the above mentioned requirements motivate that:

$$\begin{aligned} \lim_{R\to\infty} f(R) &= const., \\ \lim_{R\to 0} f(R) &= 0, \end{aligned} \tag{5.14}$$

These limits can be satisfied by a general class of broken power law models:

$$f(R) = -m^2 \frac{c_1(R/m^2)^n}{c_2(R/m^2)^n + 1}, \tag{5.15}$$

with $n > 0$, and the mass scale can be

$$m^2 \equiv \frac{\kappa^2 \bar{\rho}_0}{3} = (8315Mpc)^{-2}(\frac{\Omega_m h^2}{0.13}), \tag{5.16}$$

for convenience, where $\bar{\rho}_0 = \bar{\rho}(\ln a = 0)$ is the average density today. c_1 and c_2 are dimensionless parameters. Some examples of the model are shown below:

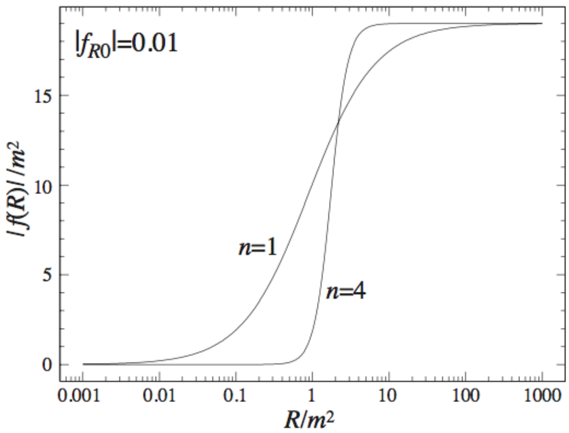

Figure 5.5: Functional form of $f(R)$ for n =1, 4 , with normalization parameters c_1 , c_2 given by $|f_{R0}| = 0.01$. $f(R)$ transition from zero to a constant as R exceeds m^2. The sharpness of the transition increases with n and its position increases with $|f_{R0}|$. During cosmological expansion, the background only reaches $R/m^2 \sim 40$ for $|f_{R0}| \ll 1$

The sign of $f(R)$ is chosen so that its second derivative

$$f_{RR} \equiv \frac{d^2 f(R)}{dR^2} > 0 \tag{5.17}$$

for $R \gg m^2$, to ensure stability of the solution at high density. There is no true cosmological constant introduced in this class. However, at curvatures high compared with m^2, $f(R)$ can be expanded as

$$\lim_{m^2/R \to 0} f(R) \approx -\frac{c_1}{c_2} m^2 + \frac{c_1}{c_2^2} m^2 (\frac{m^2}{R})^n \tag{5.18}$$

Thus, the limiting case of $c_1/c_2^2 \to 0$ at fixed c_1/c_2 is a cosmological constant in both cosmological and local tests of gravity. Moreover, at finite c_1/c_2^2, the curvature freezes into a fixed value and ceases to decline with the matter density, creating a class of models that accelerate in a manner similar to ΛCDM. While these models can accelerate the expansion, they evolve in the future into an unstable regime where $1 + f_R < 0$ and also do not contain ΛCDM as a limiting case of the parameter space.

5.3.1 Background Evolution Equations

Variation of the action (5.14) with respect to the metric yields the modified Einstein equations

$$G_{\alpha\beta} + f_R R_{\alpha\beta} - (\frac{f}{2} - \Box f_R) g_{\alpha\beta} - \nabla_\alpha \nabla_\beta f_R = \kappa^2 T_{\alpha\beta}, \tag{5.19}$$

where the field is described by,

$$f_R \equiv \frac{df(R)}{dR}. \tag{5.20}$$

Since $f(R)$ modifications only appear at low redshift, we take a matter-dominated stress-energy tensor. For the background FLRW metric,

$$R = 12H^2 + 6HH', \tag{5.21}$$

where $H(\ln a)$ is the Hubble parameter and $' \equiv d/d\ln a$. This gives us the modified Friedmann equation:

$$H^2 - f_R(HH' + H^2) + \frac{1}{6}f + H^2 f_{RR}R' = \frac{\kappa^2\bar{\rho}}{3}. \tag{5.22}$$

To solve these equations, we re-express them in terms of parameters whose values vanish in the high redshift limit where $f(R)$ modifications are negligible.

$$\begin{aligned} y_H &\equiv \frac{H^2}{m^2} - a^{-3}, \\ y_R &\equiv \frac{R}{m^2} - 3a^{-3} \end{aligned} \tag{5.23}$$

Equations (5.21) and (5.22) become a coupled set of ordinary differential equations

$$y'_H = \frac{1}{3}y_R - 4y_H, \tag{5.24}$$

$$y'_R = 9a^{-3} - \frac{1}{y_H + a^{-3}}\frac{1}{m^2 f_{RR}} \times [y_H - f_R(\frac{1}{6}y_R - y_H - \frac{1}{2}a^{-3}) + \frac{1}{6}\frac{f}{m^2}]. \tag{5.25}$$

To complete this system, we take the initial conditions at high redshift to be given by detailed balance of perturbative corrections to $R = \kappa^2\rho$. Thus, the impact of $f(R)$ on the expansion history can be recast as an effective equation of state for a dark energy model with the same history:

$$1 + w_{eff} = -\frac{1}{3}\frac{y'_H}{y_H} \tag{5.26}$$

5.3.2 Expansion History

The Hu-Sawicki $f(R)$ models in Eq. (5.15) yield expansion histories that are observationally viable, i.e. that deviate from ΛCDM in the effective equation of state (5.26) by no more than $|1 + w_{eff}| \lesssim 0.2$ during the acceleration epoch. This is the same as choosing a value for the field at the present epoch $f_{R0} \equiv f_R(\ln a = 0) \ll 1$ or, equivalently, $R_0 \gg m^2$. In this case, the approximation of Eq. (5.18) applies for the whole past expansion history and the field is always near the minimum of the effective potential

$$R = \kappa^2\rho - 2f \approx \kappa^2\rho + 2\frac{c_1}{c_2}m^2, \tag{5.27}$$

where the $2f$ term is nearly constant and mimics the energy density of a cosmological constant. Thus, to approximate the expansion history of ΛCDM with a cosmological constant $\tilde{\Omega}_\Lambda$ and matter density $\tilde{\Omega}_m$ with respect to a fiducial critical value,

$$\frac{c_1}{c_2} \approx 6\frac{\tilde{\Omega}_\Lambda}{\tilde{\Omega}_m} \tag{5.28}$$

leaving two remaining parameters, n and $c_1/c_2^2 = 6\tilde{\Omega}_\Lambda/c_2\tilde{\Omega}_m$ to control how closely the model mimics ΛCDM. Larger n mimics ΛCDM until later in the expansion history; smaller c_1/c_2^2 mimics it more closely. $\tilde{\Omega}_m$ is only the true value in the limit since it does not depend on the f_R modification, unlike the critical density and Hubble parameter.

$$\lim_{c_1/c_2^2 \to 0} \tilde{\Omega}_m = \Omega_m \tag{5.29}$$

For the flat ΛCDM expansion history:

$$R \approx 3m^2(a^{-3} + 4\frac{\tilde{\Omega}_\Lambda}{\tilde{\Omega}_m}) \tag{5.30}$$

and the field becomes:

$$f_R = -n\frac{c_1}{c_2^2}(\frac{m^2}{R})^{n+1}. \tag{5.31}$$

At the present epoch

$$\begin{aligned} R_0 &\approx m^2(\frac{12}{\tilde{\Omega}_m} - 9), \\ f_{R0} &\approx \; -n\frac{c_1}{c_2^2}(\frac{12}{\tilde{\Omega}_m} - 9)^{-n-1}. \end{aligned} \tag{5.32}$$

In particular, for $\tilde{\Omega}_m = 0.24$ and $\tilde{\Omega}_\Lambda = 0.76$, $R_0 = 41m^2$, $f_{R0} \approx -nc_1/c_2^2/(41)^{n+1}$ for $|f_{R0}| \ll 1$. The consequences of cosmological and solar system-tests can be phrased in a nearly model-independent way by quoting the field value f_R. Consequently, we will hereafter parameterize the amplitude c_1/c_2^2 through the cosmological field value today, f_{R0}.

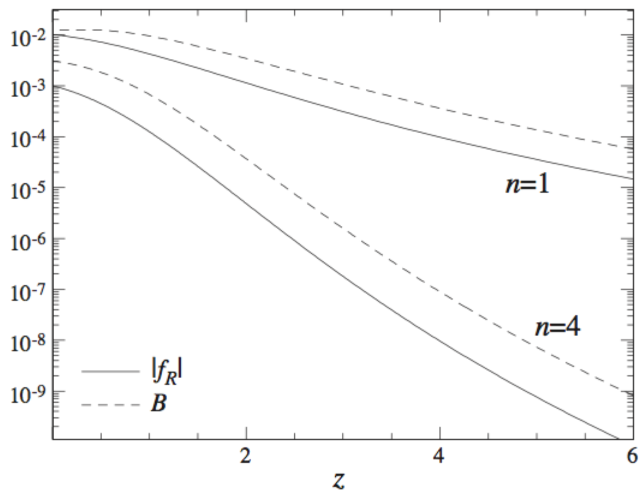

Figure 5.6: Cosmological evolution of the scalar field f_R and the Compton wavelength parameter B for models with n = 1, 4. Deviations from general relativity decline rapidly with redshift as n increases.

Figure 5.6 shows several examples of the background evolution of f_R. For a fixed present value f_{R0}, a larger n produces a stronger suppression of the field at high redshift. The effective equations of state for these models are shown in Figure 5.7. Deviations from a cosmological constant, $w_{eff} = -1$, are of the same order of magnitude as f_{R0}. The Hu-Sawicki class of models has a phantom effective equation of state, $w_{eff} < -1$, at high redshift and crosses the phantom divide at a redshift that decreases with increasing n.

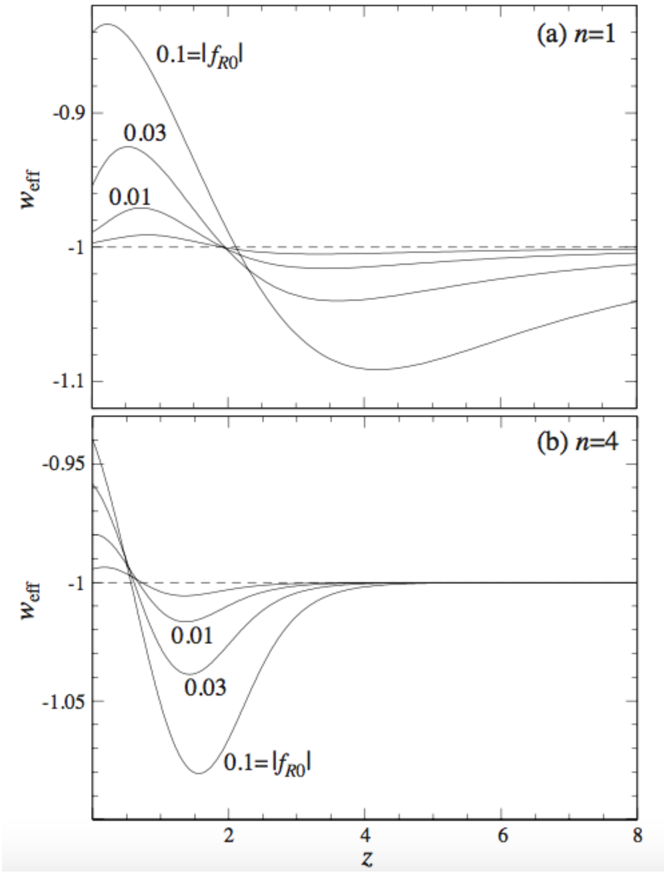

Figure 5.7: Evolution of the effective EoS for n = 1, 4 for several values of f_{R0}. The effective EoS crosses the phantom divide $w_{eff} = -1$ at a redshift that decreases with increasing n.

In the high curvature limit of the Hu-Sawicki models, the function reads:

$$f(R) = R - 2\Lambda + |f_{R0}| \frac{\bar{R}^{n+1}}{R^n}, \tag{5.33}$$

where $\bar{R}$ is the curvature today. This model requires an effective cosmological constant to explain the observed accelerated expansion of the universe. However, it is possible to find a function $f(R)$ so that this constant disappears in the low curvature limit. The correction to the ΛCDM disappears in the high curvature limit $R \gg \bar{R}$. The Solar System constraint imposes the condition $|f_{R0}| < 10^{-6}$. Also, the background cosmology is indistinguishable from ΛCDM scenario if $|f_{R0}|$ is small. In the next section, we discuss some f(R) halo mass function models that use the Hu-Sawicki parameterization of $f(R)$.

5.4 Halo Model Modification

In this section of the thesis, we look at the modification of halo mass function for $f(R)$ gravity, as proposed by [3]. In [3], they compute the critical density of collapse for spherically symmetric overdensities in a Hu-Sawicki-Starobinsky $f(R)$ gravity model:

$$f(R) = -2\Lambda + \frac{\epsilon}{n}\frac{(4\Lambda)^{n+1}}{R^n} \tag{5.34}$$

where [3] fix $n = 1$ to get their fitting functions, Λ is a constant energy scale whose value coincides with the measured value $\Lambda = \Lambda_{obs} = 3H_0^2\Omega_\Lambda$ and $\epsilon \ll 1$ is a small positive deformation parameter which is related to the more commonly used f_{R0}, via

$$f_{R0} \equiv \epsilon(1 + \frac{1}{4}(\Omega_\Lambda^{-1} - 1))^{-(n+1)} \tag{5.35}$$

To get the spherical collapse critical density, [3] evolve the Einstein, scalar field and non-linear fluid equations and solve them numerically. They only make a minimal simplifying assumption that the metric potentials and scalar field remain quasi-static throughout the collapse. This is necessary due to the breakdown of Birkhoff's theorem in $f(R)$ scenario, which states that a spherically symmetric solution of the vacuum Einstein equations is always static in a region where the time coordinate remains time-like and spatial coordinates stay space-like. They found that the density threshold for collapse depends significantly on the initial conditions imposed while evolving a top hat profile. Hence, they imposed some 'natural' initial conditions, and obtained a fitting function for the spherical collapse critical density, $\delta_c(M, z, f_{R0})$, as a function of collapse redshift, mass of the overdense region within the model parameter range $10^{-7} < f_{R0} < 10^{-4}$. For the initial condition, they use the average density profile around a density peak which is completely determined by the input cosmology. Consequently, this removes any ambiguity in the choice of initial profile and makes the spherically symmetric setup as physically accurate as possible. They further employ the drifting and diffusing barrier within the context of excursion set theory, so as to model aspherical collapse, to get a more realistic δ_c and halo mass function $n(M, z, \delta_c, f_{R0})$. Their proposed analytic formula for the halo mass function matched well against Monte Carlo random walks for a wide class of moving barriers. In the next chapter, we use these fitting functions to present our results both for spherical and aspherical case. As such, the results of this thesis are largely based on the prescriptions described in [3].

5.4.1 $f(R)$ Spherical Collapse

In Section 4.2.1, we discussed the basics of spherical collapse of overdense regions in ΛCDM gravity, and developed the equations for it. In GR, the calculation of δ_c is quite simple because an initially homogeneous top-hat overdensity retains its shape during collapse, by the virtue of the Birkhoff's theorem. This allows us to treat the size of the homogeneous overdense region as the scale factor of a closed FRW universe. However, in $f(R)$ theories, the additional scalar degree of freedom allows for monopole radiation, thus Birkhoff's theorem no longer applies.

A more severe problem is that the gravitational force is scale dependent in the linear regime of collapse due to mass of the fluctuations. Finally, the gravitational force depends on the local density since the chameleon mechanism starts to take effect because the energy density is large enough during the collapse. As a result of these effects, an initial top-hat overdensity does not retain its shape during collapse and we cannot use a closed FRW to describe its collapse. Rather, we must solve the spherically symmetric $f(R)$ field equations, which have been reduced to the set of nonlinear field and fluid equations presented in Eq. (26a-26d) of [3]. They consider the chameleon screening mechanism in their approach. In [3], they don't consider the effects of halos being composed of subhalos, which increases the chameleon effect, and of forming cluster itself being a subcluster of a larger sized over/underdensity, which enhances/diminishes the chameleon effect. They do however taken into account part of the environmental dependence of the collapse threshold by using the average density profile around a peak, which only depends on linear power spectrum $P(z_i, k)$. They use the fully non-linear metric below to admit a spherically symmetric spatial slicing:

$$ds^2 = -e^{2\Phi}dt^2 + a^2e^{-2\Psi}(dr^2 + r^2d\Omega^2), \tag{5.36}$$

where both Φ and Ψ are functions of r and t.

They take $z_i = 500$ to be the initial time for the spherical collapse. At this redshift, radiation is already sub-dominant relative to matter by a factor of order $\sim \mathcal{O}(0.1)$. [3] uses CAMB to obtain $\sigma(z = 0, R)$ with the choice of cosmological parameters: $\sigma_8 = 0.8$, $\Omega_m = 0.27$, $h = 0.7$, $n_s = 0.96$, and then evolve the general relativistic growth equation to obtain $\sigma(z_c, R) = D(z_c)\sigma(z = 0, R)$ to the collapse redshift, neglecting radiation.

The main results of [3] are the $f(R)$ collapse threshold δ_c and a realistic halo mass function $n(M)$ as a function of f_{R0}, z and M. They first obtain δ_c as a fit function from numerical solutions of the field equations, and then use it by adding a drifting and diffusing barrier in the excursion set theory to obtain a realistic mass function $n(M)$.

The threshold for collapse is be a non-linear function of the $f(R)$ model parameters n and f_{R0}, and also the initial density δ_i (or z_c), and the mass of the overdensity M. They fix n = 1 for simplicity. [3] observed a clear linear dependence between δ_c and $\log_{10}[M/(M_\odot h^{-1})]$ for small M and a z and f_{R0}-dependent break in this behavior [Figure 6 of [3]]. This break is determined by $m_b = 0$ from Eq. (5.37). δ_c also approaches to the GR value δ_c^Λ for increasing z_c, and also for $f_{R0} = 0$ limit, $\delta_c \to 1.686$. They also find an approximately linear relationship between δ_c and $\log[M/M_\odot]$ for $f_{R0} \gtrsim 10^{-5}$. The fitting function for δ_c that they provide is given by:

$$\begin{aligned}
\delta_c(z, M, f_{R0}) &= \delta_c^\Lambda(z)[1 + b_2(1+z)^{-a_3}(m_b - \sqrt{m_b^2 + 1}) + b_3(\tanh m_b - 1)], \\
m_b(z, M, f_{R0}) &= (1+z)^{a_3}(\log_{10}[M/(M_\odot h^{-1})] - m_1(1+z)^{-a4}), \\
m_1(f_{R0}) &= 1.99 \log_{10} f_{R0} + 26.21, \\
b_2 &= 0.0166, \\
b_3(f_{R0}) &= 0.0027 \times (2.41 - \log_{10} f_{R0}), \\
a_3(f_{R0}) &= 1 + 0.99 \exp[-2.08(\log_{10} f_{R0} + 5.57)^2], \\
a_4(f_{R0}) &= (\tanh[0.69 \times (\log_{10} f_{R0} + 6.65)] + 1)0.11.
\end{aligned} \tag{5.37}$$

The fit function converges separately for $M \to \infty$ and $z \to \infty$ to its GR limit $\delta_c^\Lambda(z)$, which can be approximated by [48]:

$$\delta_c^\Lambda(z) \simeq \frac{3(12\pi)^{2/3}}{20}(1 - 0.0123\log_{10}[1 + \frac{\Omega_m^{-1} - 1}{(1+z)^3}]) \tag{5.38}$$

The result (5.37) above was deduced by considering a_3, a_4, b_2, b_3, m_1 as independent fit parameters for each f_{R0} value. The parameter m_1 is of particular interest since it determines the position of the chameleon transition at z = 0, where $\delta_c(M)$ changes its behavior from a linear growth in $\log M$ to a constant [Figure 6 of [3]]. Therefore roughly speaking the halo mass function at $z = 0$ approaches ΛCDM for masses larger than

$$M_1 = 10^{14.2}(\frac{f_{R0}}{10^{-6}})^2 M_\odot h^{-1} \tag{5.39}$$

due to the chameleon mechanism.

5.4.2 $f(R)$ Halo Mass Function

We discussed the halo mass function for ΛCDM scenario in Section 4.2.2. Here we see how it looks in f(R) gravity scenario. As we know, dark matter halos are formed from non-linear collapse of initial density perturbations. The initial matter density field and the collapse threshold determine the abundance of the virialized clusters. The excursion set approach computes the abundance of dark matter halos as a function of their mass. It requires smoothing the initial density field over different realizations, which collapses once the overdensity in the smoothing region is above a threshold. Thus, the halo mass function $n(M)$, which is the number density of halos in the mass range $[M, M + dM]$, is given by:

$$n(M) = f(\sigma)\frac{\bar{\rho}_0}{M^2}\frac{d\ln\sigma^{-1}}{d\ln M}, \tag{5.40}$$

where $\bar{\rho}_0$ is the comoving background dark matter density and $f(\sigma)$ is multiplicity function, which is the fundamental quantity containing all information about the non-linear collapse.

In the case of spherically collapsing overdensities, the Press-Schechter (PS) approach defines the multiplicity function as:

$$f(\sigma) = \sqrt{\frac{2}{\pi}}e^{-\delta_c^2/(2\sigma^2)}\frac{\delta_c}{\sigma}, \tag{5.41}$$

The dynamics of collapse in the real universe is not spherical though. We can therefore modify the expression for $f(R)$ models with realistic collapse parameters. Using ellipsoidal collapse in the excursion set approach introduces a stochastic barrier, which motivates us to consider a generic barrier. In the ΛCDM case, it is sufficient to take a simple Gaussian distribution for the barrier B with a mean value $\bar{B}$ drifting linearly as function of the variance S. But for $f(R)$ gravity, we cannot use a linear barrier to model the spherical collapse. To obtain an analytical expression for $f(\sigma)$, we consider a generic barrier. In the case where $\bar{B} = \delta_c + \beta S$, the multiplicity function becomes:

$$f(\sigma) = \sqrt{\frac{2a}{\pi}}e^{-a\bar{B}^2/(2\sigma^2)}\frac{\delta_c}{\sigma}, \tag{5.42}$$

with $a = 1/(1 + D_B)$. For generic $\bar{B}(S)$, [3] model the spherical collapse barrier for $f(R)$ by using:

$$f(\sigma) = \sqrt{\frac{2a}{\pi}} e^{-a\bar{B}^2/(2\sigma^2)} \frac{1}{\sigma} (\bar{B} - S\frac{d\bar{B}}{dS}), \tag{5.43}$$

They checked this fit with Monte Carlo predictions and found a difference of order $\sim 5\%$, confirming it to be an excellent fit.

Since we don't have N-body simulations, one way to evaluate the effect of $f(R)$ gravity on the halo mass function is to use spherical collapse (ie: $D_B = 0, \beta = 0$) and measure the ratio between the GR and $f(R)$ prediction for an uncorrelated walk (ie: sharp-k filter). [3] makes an argument to instead consider a real-space top-hat filter (i.e., sharp-x), which induces non-Markovian corrections whose magnitude is given by κ, which depends on the linear matter power spectrum. For a ΛCDM universe, $\kappa \sim 0.65$. This formalism has been applied to a stochastic barrier with Gaussian distribution and the solution has been extended to a diffusive barrier with mean $\delta_c + \beta S$. Such a barrier can describe the main features of ellipsoidal collapse quite well. In such a case, the multiplicity function to first order in κ is given by:

$$f(\sigma) = f_0(\sigma) + f^{m-m}_{1,\beta=0}(\sigma) + f^{m-m}_{1,\beta^{(1)}}(\sigma) + f^{m-m}_{1,\beta^{(2)}}(\sigma), \tag{5.44}$$

where,

$$f_0(\sigma) = \frac{\delta_c}{\sigma}\sqrt{\frac{2a}{\pi}} e^{-\frac{a}{2\sigma^2}(\delta_c + \beta\sigma^2)^2} \tag{5.45}$$

$$f^{m-m}_{1,\beta=0}(\sigma) = -\tilde{\kappa}\frac{\delta_c}{\sigma}\sqrt{\frac{2a}{\pi}}[e^{-a\delta_c^2/(2\sigma^2)} - \frac{1}{2}\Gamma(0, \frac{a\delta_c^2}{2\sigma^2})], \tag{5.46}$$

$$f^{m-m}_{1,\beta^{(1)}}(\sigma) = -a\delta_c\beta[\tilde{\kappa}\,\mathrm{Erfc}(\delta_c\sqrt{\frac{a}{2\sigma^2}}) + f^{m-m}_{1,\beta=0}(\sigma)], \tag{5.47}$$

$$f^{m-m}_{1,\beta^{(2)}}(\sigma) = -a\beta[\frac{\beta}{2}\sigma^2 f^{m-m}_{1,\beta=0}(\sigma) + \delta_c f^{m-m}_{1,\beta^{(1)}}(\sigma)]. \tag{5.48}$$

In [33] it was shown that the first order in κ is sufficient to reproduce the exact solution to $\sim 5\%$ accuracy, using parameter values $\beta = 0.12, D_B = 0.4$. This effective barrier can match the N-body halo mass function with accuracy $\sim 5\%$ and is also consistent with the collapse threshold. This suggests that β , D_B are parameters that should depend on physics of the collapse dynamics. It is not clear how $f(R)$ gravity effects the collapse of an aspherical patch. However, we can assume for $f_{R0} \to 0$ one should recover the GR limits. As an initial step, [3] fixed β and D_B to their GR values and ran Monte Carlo walks for the sharp-x filter, with δ_c given by (5.37). We start by trying to predict the multiplicity function for $f(R)$ gravity. Note that the sharp-x multiplicity function can be rewritten as the sharp-k function with a correction in κ. Hence the ratio between the GR and $f(R)$ predictions is given by:

$$\frac{f^{f(R),sx}}{f^{GR,sx}} = \frac{f^{f(R),sk} + f^{f(R)}_{\kappa=1} + \mathcal{O}(\kappa^2)}{f^{GR,sk} + f^{GR}_{\kappa=1} + \mathcal{O}(\kappa^2)} \tag{5.49}$$

where $f^{GR,sk}$ is given by Eq. (5.45), $f^{GR,sx}$ by Eq. (5.44), $f^{f(R),sk}$ by Eq. (5.43), $f^{GR}_{\kappa=1}$ by Eq. (5.46-5.48) and $f^{f(R)}_{\kappa=1}$ is the first order non-Markovian corrections due to the sharp-x filter. Expanding around the GR spherical collapse solution, and ignoring the negligible quantities, [3] assumes that:

$$f^{f(R),sx}(\sigma) \simeq f^{GR,sx}(\sigma)\frac{f^{f(R),sk}}{f^{GR,sk}} \tag{5.50}$$

This assumption was tested in [3] by comparing with the exact Monte Carlo solution. Once again, the fractional difference was of order $\sim 5\%$ confirming the validity of Eq. (5.50). In this thesis, we use this simple prescription to define the multiplicity function for $f(R)$ gravity. Finally, the halo mass function can obtained from Eq. (5.50) via

$$n(M, z, f_{R0}) = f^{f(R),sx}(\sigma)\frac{\bar{\rho}_0}{M^2}\frac{d\ln\sigma^{-1}}{d\ln M} \tag{5.51}$$

As such, all the modifications in the halo mass functions in the $f(R)$ scenario is contained in the multiplicity function $f^{f(R),sx}$. This makes our analysis in this thesis very easy to compute, as we will now see in the next chapter.

Chapter 6

Results

In this section, we present our results of the critical collapse density, multiplicity functions, and SZ 1-halo and 2-halo power spectrums for different values of f_{R0} parameter in different collapse dynamics scenarios in $f(R)$ gravity. We use the Hu-Sawicki paramterization of the $f(R)$ model, as mentioned earlier. Throughout our analysis, we use WMAP9 with the following parameters as our choice of cosmology:

$$\Omega_m = 0.281,\ H_0 = 69.7,\ \Omega_b h^2 = 0.0464,\ \sigma_8 = 0.82, \text{ and } n_s = 0.971.$$

In order to predict the SZ power spectrums, we use the halo model as described in section 4.3. In the GR scenario, we use the Tinker halo mass function from section 4.2.2. To describe the $f(R)$ behavior, we use the halo mass function in Eq.(5.40) with the multiplicity function of Eq.(5.45) calibrated with the parameters $\delta_c(M)$ given in Eq.(5.37), and β, D_B that differ for spherical and aspherical collapse scenarios. As we mentioned in previous chapters, modifying halo bias and pressure profile is beyond the scope of this thesis, and hence we use the usual GR descriptions. Specifically, we use Tinker halo bias and Battaglia pressure profile. In this thesis, we are primarily interested in calculating the effect of a $f(R)$ modified halo mass function on the non-linear SZ power spectrums.

We look at clusters of masses from 10^{13} to $10^{15.5} M_\odot$ with a bin of 0.01 in $\log_{10} M$. The redshifts we are scoping range from $z = 0.02$ to $z = 5$. Starting from a non-zero redshift avoids the SZ power spectrum from being dominated by unphysical object at $z = 0$ [47]. The binning is determined by: $10H(z)/c$, where c is the speed of light: 299792.458 km/s, and $H(z) = 100\sqrt{\Omega_m(1+z)^3 + 1 - \Omega_m}$ with $\Omega_m = 0.281$. After $z = 1.5$, we increase the bin size by a factor of 2. This gives us 429 values in our z-range to integrate over.

We will be looking at f_{R0} parameters in the range $10^{-4} - 10^{-6}$. In this chapter, we only present the power spectrums for $f_{R0} = 10^{-4}, 10^{-5}, 10^{-6}$. We shall calculate the power spectrums for more f_{R0} parameter values near the fiducial ones in the next chapter to perform a signal to noise ratio (S/N) analysis.
We start by calculating the critical collapse density for all our mass, redshift, and f_{R0} samples, by using the fitting function for δ_c given in Eq. (5.37), for the above values of f_{R0}. Figure 6.1 plots the spherical collapse δ_c for a few f_{R0} model parameter values.

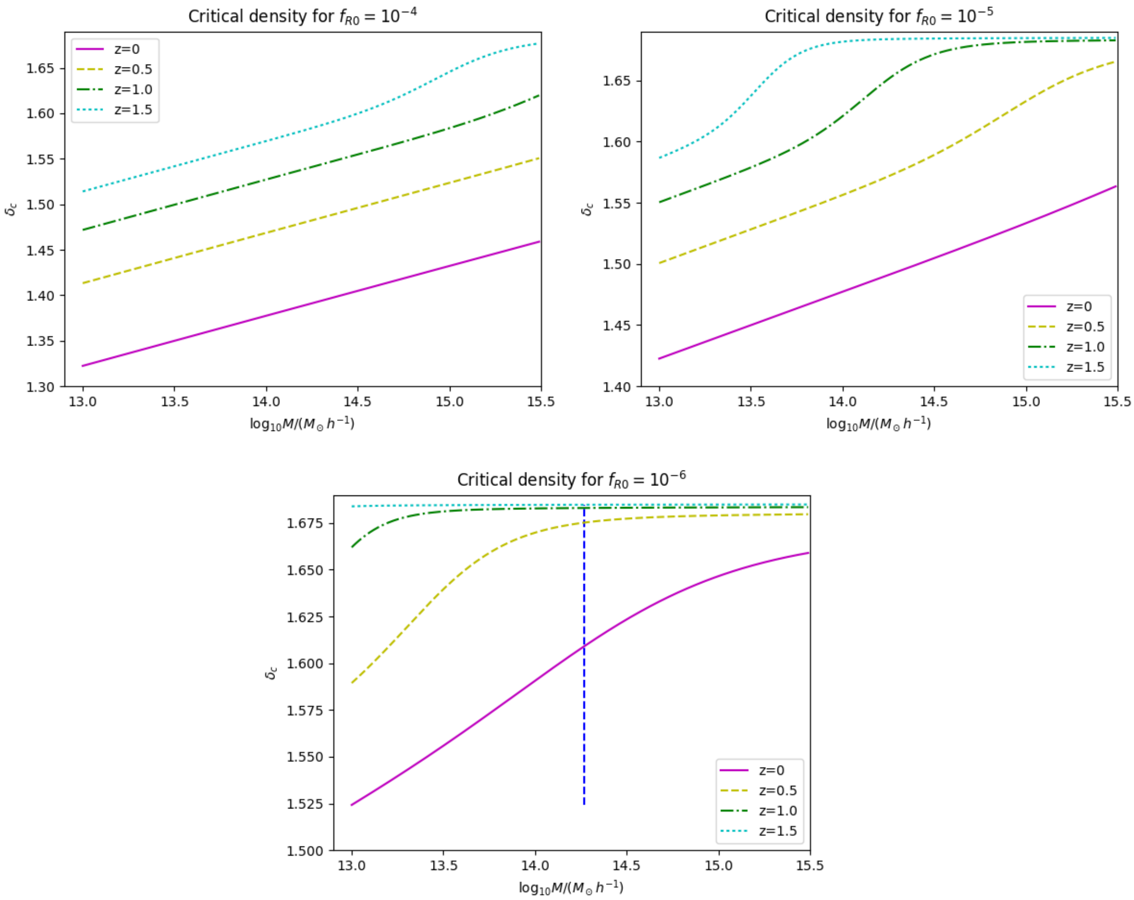

Figure 6.1: Spherical collapse δ_c as a function of $\log_{10}[M/(M_\odot h^{-1})]$ for $f_{R0} = 10^{-4}, 10^{-5}, 10^{-6}$. The lines show the fitting function Eq. (5.37). The dashed vertical line shows the mass as defined in eqn. (5.39)

There's a clear linear dependence between δ_c and $\log_{10}[M/(M_\odot h^{-1})]$ for small M. We also see a z and f_{R0}-dependent break in this linear behavior, which is determined by $m_b = 0$ from Eq. (5.37). We see that, δ_c approaches to the GR value δ_c^Λ for increasing z_c, and also for $f_{R0} = 0$ limit, $\delta_c \to 1.686$. We clearly observe a return to GR for large objects and objects with a high collapse redshift. The dashed vertical line shows the mass as defined in Eq. (5.39) for which $m_b = 0$ at $z = 0$, which tells us the position of chameleon transition at $z = 0$, where $\delta_c(M)$ changes its behavior from a linear growth in $\log M$ to a constant. We don't see a dashed line in the plots for $f_{R0} = 10^{-4}$ and 10^{-5}, since the mass from Eq. (5.39) is outside our axis range.

Having computed δ_c, we then use Eq. (5.43) to compute the spherical collapse multiplicity function $f^{f(R),sk}$ for $f_{R0} = 10^{-4}, 10^{-5}$, and 10^{-6}, for all our redshift samples. We use Eq. (5.41) to compute $f^{GR,sk}$ where we use the GR critical density from Eq. (5.38). Figure 6.2 plots the spherical multiplicity functions for a few example redshifts.

Similarly, we use Eq. (5.45) with $\beta = 0.12, D_B = 0.4$ to calculate the aspherical

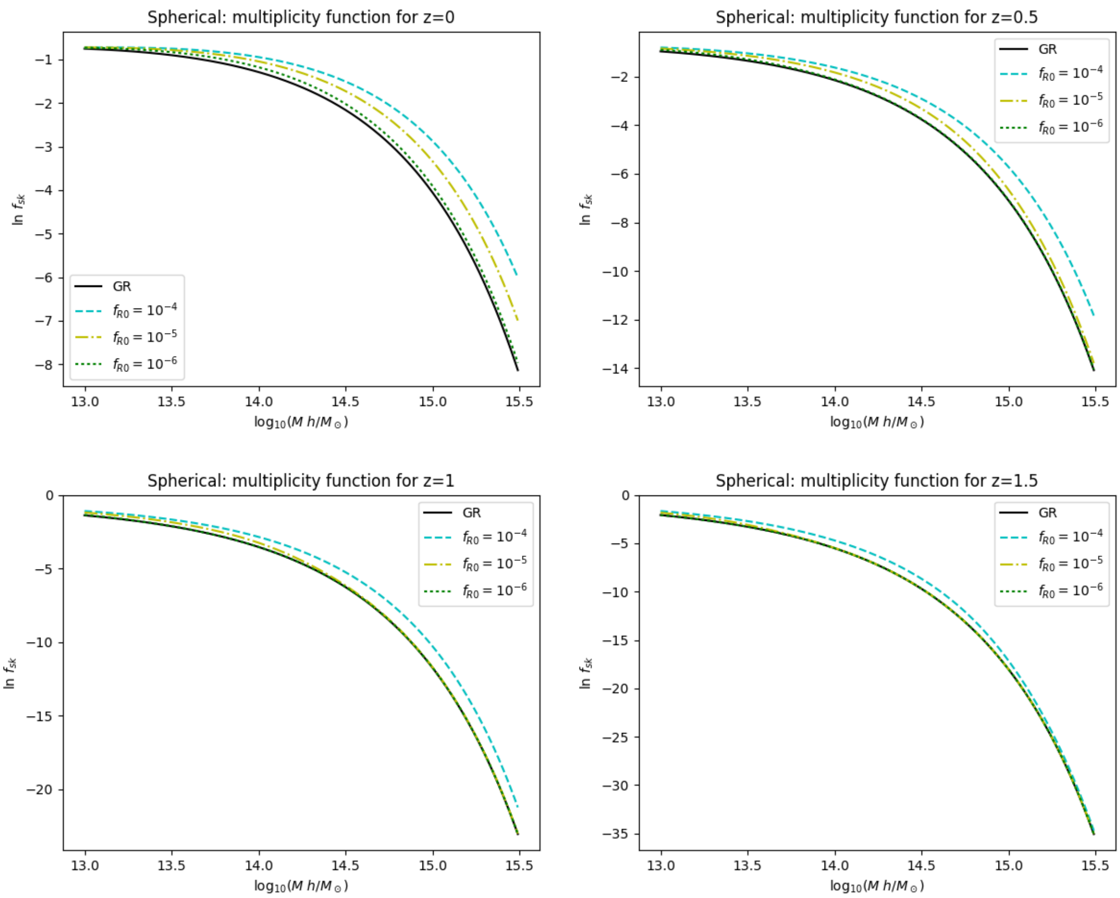

Figure 6.2: Theory (line) prediction for the f(R) multiplicity function at different redshifts using spherical collapse barrier and sharp-k filter. Solid black line shows the GR prediction while the dotted color lines are for different f_{R0}.

collapse multiplicity function $f^{f(R),sx}$ for all our mass, redshift, and f_{R0} samples. And for $f^{GR,sx}$, we just change the δ_c to the GR critical density δ_c^Λ from Eq. (5.38). A few examples are shown in Figure 6.3.

As we can see, in both collapse scenarios, we see a deviation in the multiplicity function as a function of M, z, and f_{R0}. It is evident that at higher redshifts, we approach GR. The same applies when $f_{R0} \to 0$.

Once we have computed all the multiplicity functions, we check whether there is a significant modified gravity imprint on the $f(R)$ mass function Eq. (5.51). We started by defining $\mathcal{R}^{sk}$ as the ratio between the $f(R)$ and GR multiplicity functions using the naive sharp-k and spherical collapse for three model parameters using Eq. (5.43):

$$\mathcal{R}^{sk} = \frac{f^{f(R),sk}(\delta_c^{f(R)}, \beta = 0, D_B = 0)}{f^{GR,sk}} - 1 \tag{6.1}$$

We calculate this for all our M, z, and f_{R0} samples. In Figure 6.4, we plot a few examples of this ratio over our chosen mass range for different f_{R0} model parameter values and some sample redshifts.

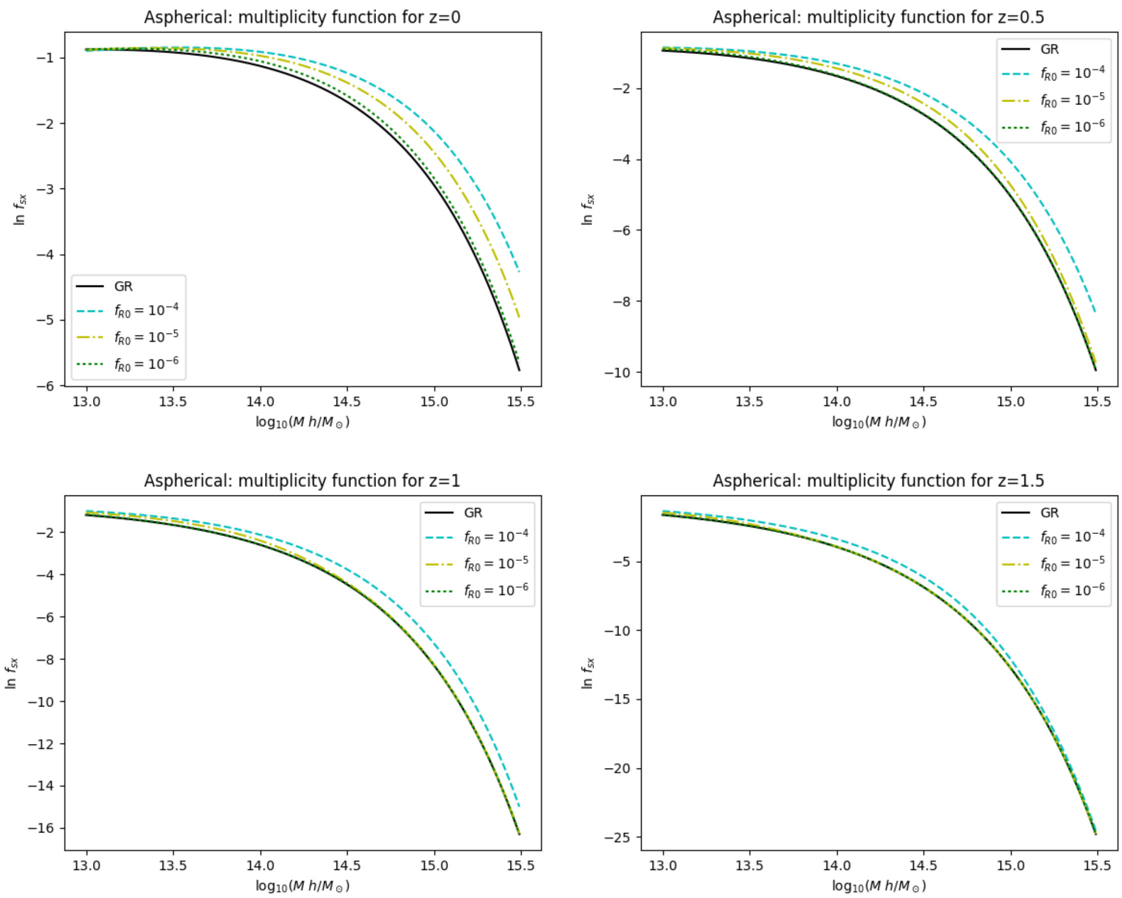

Figure 6.3: Theory (line) prediction for the f(R) multiplicity function at different redshifts using a drifting diffusing barrier and sharp-x filter. Solid black line shows the GR prediction while the dotted color lines are for different f_{R0}.

We also define $\mathcal{R}^{sx}$ as the ratio between the $f(R)$ and GR multiplicity functions using the sharp-x and aspherical collapse model:

$$\mathcal{R}^{sx} = \frac{f^{f(R),sx}(\delta_c^{f(R)}, \beta^{GR}, D_B^{GR})}{f^{GR,sx}} - 1 \tag{6.2}$$

where $f^{f(R),sx}$ is given by Eq. (5.50), $f^{GR,sx}$ is given by Eq. (5.45) using Eq. (5.38) for $\delta_c^{\Lambda}(z)$, with $D_B^{GR} = 0.4, \beta^{GR} = 0.12$. As evident from Eq. (5.50), and discussed earlier, the first order $f^{f(R),sk}$ in κ is sufficient to reproduce the exact solution for $f^{f(R),sx}$ to $\sim 5\%$ accuracy, using parameter values $\beta = 0.12, D_B = 0.4$. We use this approximation to plot $\mathcal{R}_{sx}$ for different f_{R0} model parameter values in Figure 6.5.

We see that both $\mathcal{R}_{sx}$ and $\mathcal{R}_{sk}$ share the same qualitative features. As such, Figure 6.4 and 6.5 basically show us the number count ratio for various f_{R0} values and their evolution at different redshifts. It is clear that the $f(R)$ signature strongly depends on redshift. Moreover, there is a distinctive signature in both the mass and time dependence of the halo mass function due to the chameleon effect. We can also see that modified gravity effects are suppressed for models

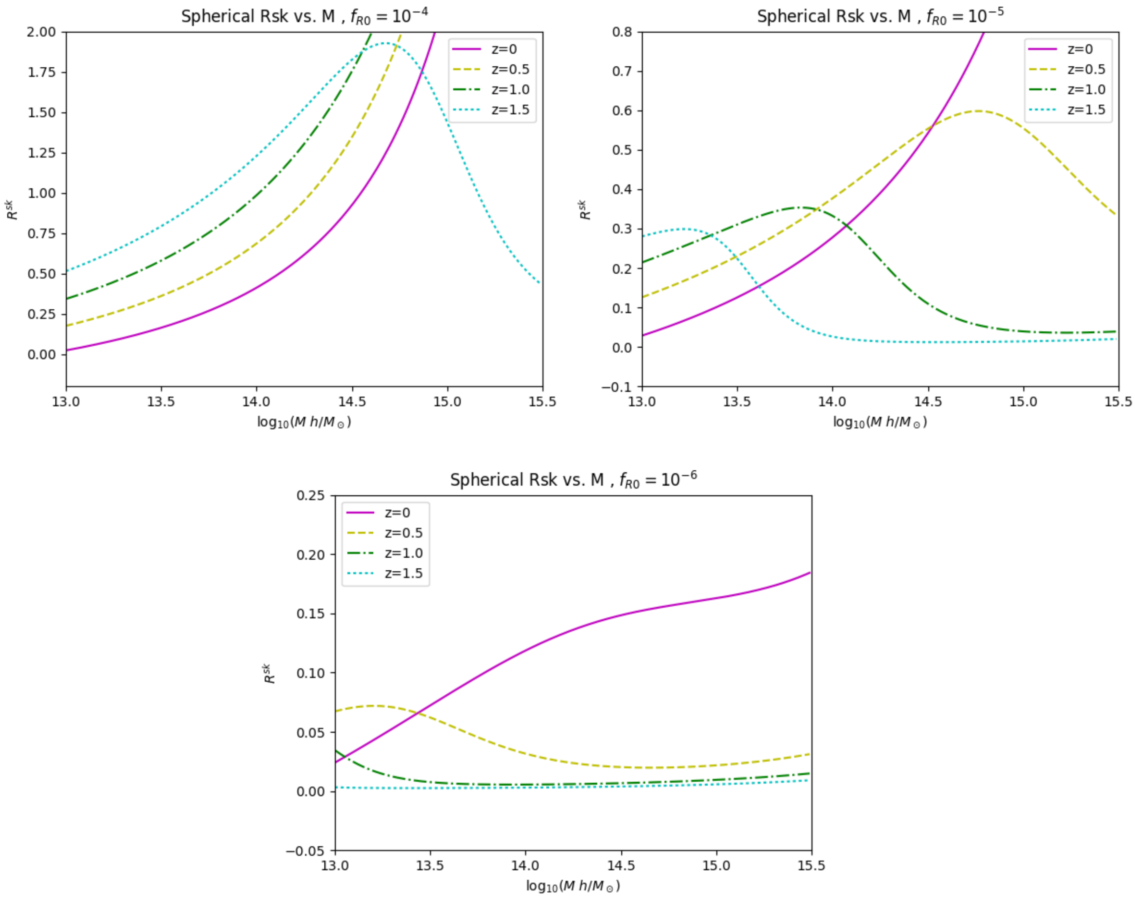

Figure 6.4: Multiplicity function ratio R between GR and $f(R)$ gravity over different redshift and f_{R0} parameters for naive spherical collapse with sharp-k filter.

with f_{R0} values close to that for GR, suggesting that below $f_{R0} \sim \mathcal{O}(10^{-6})$, we cannot competitively use cluster counts to probe modified gravity.

From Eq. (5.51), it follows that:

$$\mathcal{R}^{sx} = \frac{n^{f(R),sx}(\delta_c^{f(R)}, \beta^{GR}, D_B^{GR})}{n^{GR,sx}} - 1 \tag{6.3}$$

where n is the halo mass function. Hence, we can use Eq. (5.50) in Eq. (5.40) to study how the number count of halos changes for $f(R)$ gravity compared to GR. In Figure 6.6, we show some examples of halo mass functions obtained by multiplying the ratio $(\mathcal{R}_{sk} + 1)$ and $(\mathcal{R}_{sx} + 1)$ to the GR halo mass function for spherical and aspherical collapse scenarios respectively. The GR halo mass function was calculated using the *hmf* python module for the earlier mentioned cosmology. We only show plots for $f_{R0} = 10^{-4}$ and redshifts $z = 0.02$ and 1.5.

As we can see, the $f(R)$ halo mass function of aspherical collapse is lower than that of spherical collapse. This tells us that spherical collapse slightly overestimates the number count of halos. We also note that $f(R)$ gravity predicts a boost in the number counts of massive clusters at lower redshifts. Also, for high redshifts,

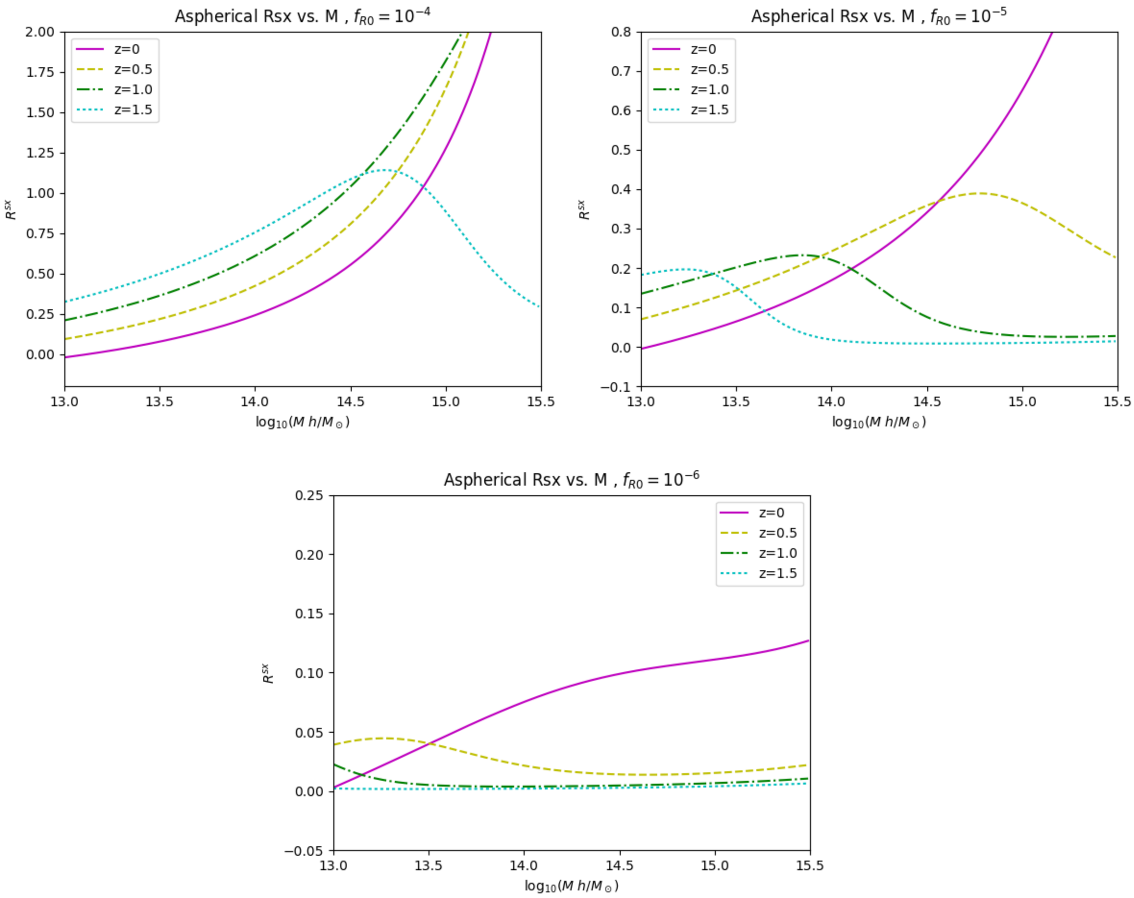

Figure 6.5: Multiplicity function ratio R between GR and $f(R)$ gravity over different redshift and f_{R0} parameters for a drifting diffusive barrier with sharp-x filter.

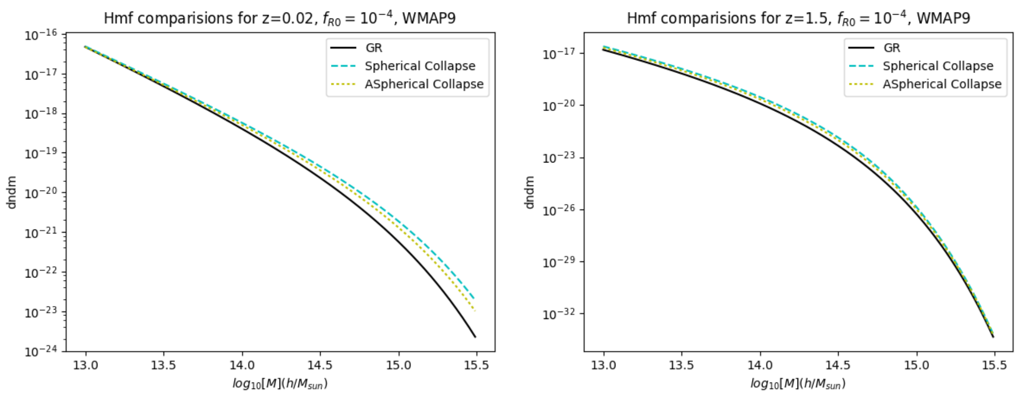

Figure 6.6: Comparison of halo mass functions in GR, $f(R)$ spherical, f(R) aspherical cases for redshifts z=0.02 and z=1.5 for $f_{R0} = 10^{-4}$

we note the deviation from GR becoming minimal.

Once we have calculated the factors $(\mathcal{R}^{sk} + 1)$ and $(\mathcal{R}^{sx} + 1)$ to modify our GR halo mass functions for our interested mass and redshift range, we have the ingredients to calculate the SZ power spectrums. We assumed a GR gravity for redshifts above $z = 1.5$, i.e., our $\mathcal{R}^{sk}$ and $\mathcal{R}^{sx}$ are zero above $z = 1.5$. Figure 6.7 shows us the power spectrums in spherical and aspherical collapse scenario for GR, $f_{R0} = 10^{-4}, 10^{-5}$, and 10^{-6} gravities.

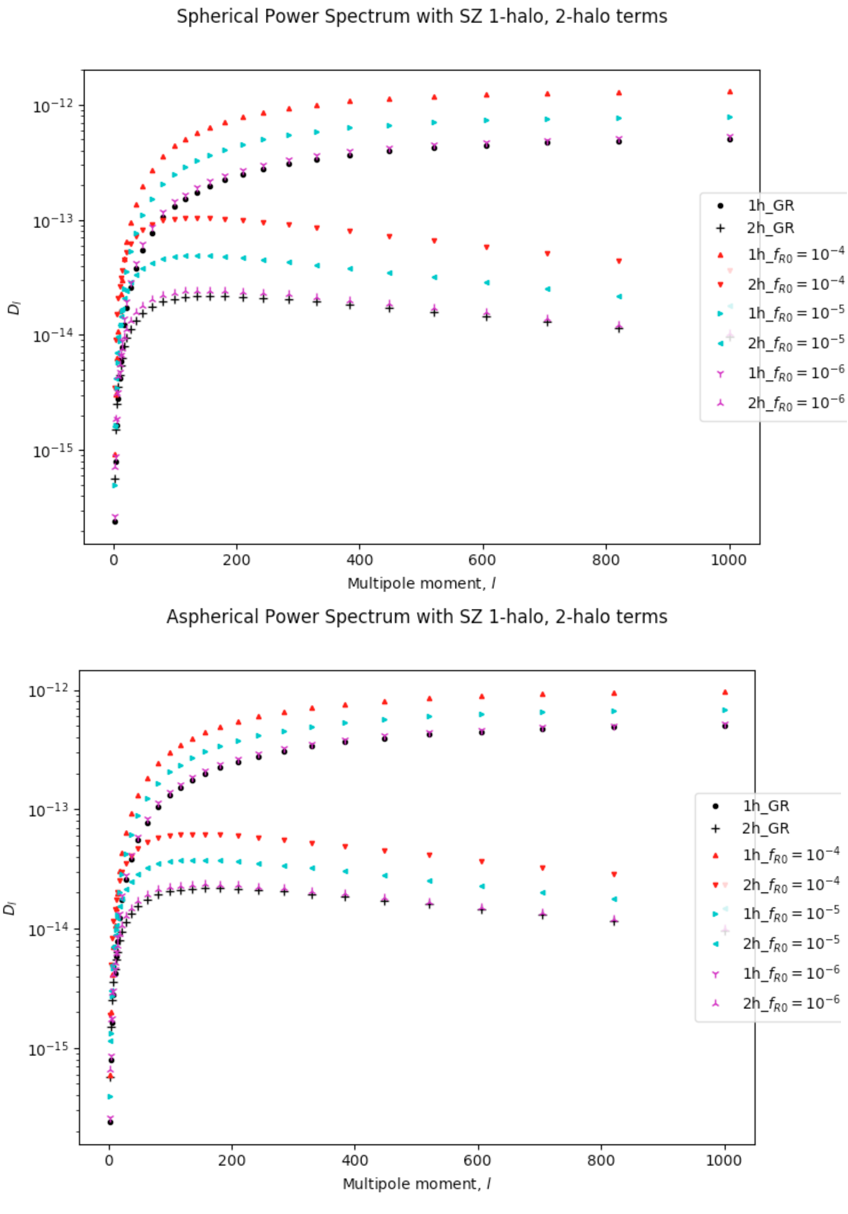

Figure 6.7: SZ Power Spectrum for spherical and aspherical collapse scenarios showing the 1-halo and 2-halo terms.

The y-axis $D_l = l(l+1)C_l/2\pi$. We are calculating the spectrum up to multipole $l = 1000$, as above this, the noise is considerably high in our current and proposed future experiments (Planck, PIXIE, and PRISM). Moreover, most of our signal will come from very low multiples (i.e. large scales) since $f(R)$ gravity is best tested by halo distribution on large scales. We confirm this in the next chapter. The 1-halo and 2-halo terms of SZ power spectrums were calculated using a code that integrates Eq. (4.39-4.41) in the Limber approximation.

As expected, a change in the gravity theory does indeed change the SZ power spectrum. Moreover, we can see that $f(R)$ theory with $f_{R0} = 10^{-4}$ shows the highest deviation from GR, and that it approaches GR as $f_{R0} \to 0$. We would like to quantify this signal in the context of experiments, which motivates a signal to noise ratio (S/N) forecast in the next chapter for upcoming experiments.

Chapter 7

Fisher Forecast

In this chapter, we will be doing a S/N computation for PRISM and PIXIE experiments. We also compute S/N for a theoretical cosmic variance limited experiment, for reference.
Before we begin computing the S/N ratios, we'd like to point out that the power spectra in the previous chapter were only computed for some multipole values, l, between 2 and 1000, to save computation time. To get an accurate prediction of S/N, we must add the contributions from all multipoles. Therefore, we do a cubic spline interpolation of the 1-halo and 2-halo terms of the SZ power spectrum for every l. For this, we use the *scipy.interpolate* python module. Figure 7.1 shows the interpolations performed for GR and $f(R)$ gravities.

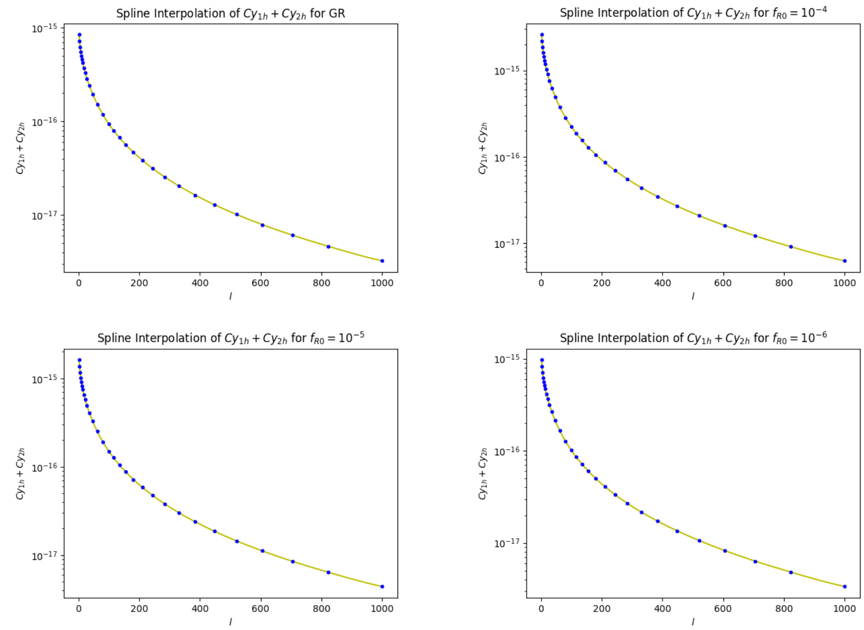

Figure 7.1: Interpolation of C_l values for every l. The dots represent the values actually computed.

As we can see, the interpolation fits the computed values very well. Having done this, we continue first with a simple S/N computation using the formula:

$$\frac{S}{N} = \sqrt{\sum_l (2l+1) \frac{(C_l^{yy,f(R)} - C_l^{yy,GR})^2}{(max[C_l^{yy,f(R)}, C_l^{yy,GR}] + N_l)^2}} \tag{7.1}$$

where, N_l is the expected noise spectrum (C_l^{noise}) of the experiment, and the factor $(2l+1)$ comes from fact that we are mediating the $a_{l,m}$ over all the $m = -l, .., l$ to calculate the C_l. $N_l = 4\pi(1.4 \times 10^{-8})^2 e^{l^2/84^2}$ for PIXIE and $N_l = 4\pi \times 10^{-18} e^{l^2/100^2}$ for PRISM, [44] [45] and $N_l = 0$ for a theoretical cosmic variance limited experiment. The results from this computation are given below:

f_{R0}	CVLE	PRISM	PIXIE
10^{-4}	504.193	76.614	7.497
10^{-5}	294.195	46.134	3.579
10^{-6}	43.650	8.353	0.538

Table 7.1: S/N for different f_{R0} parameter values for up-coming PRISM and PIXIE experiments. CVLE refers to a cosmic variance limited experiment.

A much better way to compute S/N is by doing a Fisher forecast. The Fisher matrix is defined as:

$$F_{ij} \equiv \left\langle \frac{\partial L \partial L}{\partial p_i \partial p_j} \right\rangle \tag{7.2}$$

where L is the logarithm of the likelihood and p are the free parameters of the theory. In our case, it is equivalent to:[36]

$$F_{ij} = \sum_l (\mathbf{Cov}_l^{-1})_{\alpha\beta} \frac{\partial(\mathbf{Cov}_l)_{\beta\gamma}}{\partial p_i} (\mathbf{Cov}_l^{-1})_{\gamma\delta} \frac{\partial(\mathbf{Cov}_l)_{\delta\alpha}}{\partial p_j} \tag{7.3}$$

where $\mathbf{Cov}_l$ is the covariance matrix and repeated matrix indices $(\alpha, ..., \delta)$ are summed. The $f(R)$ Fisher matrix in our case reads:

$$(\frac{S}{N})^2 = F = \sum_l (2l+1) \frac{(\frac{\partial C_l}{\partial f_{R0}})^2}{(C_l + N_l)^2} \tag{7.4}$$

To get the partial derivatives around our fiducial values of $f_{R0} = 10^{-4}, 10^{-5}$, and 10^{-6}, we need to evaluate the SZ power spectrums near our fiducial values. Figure 7.2 shows the points for which we computed power spectrums. To compute

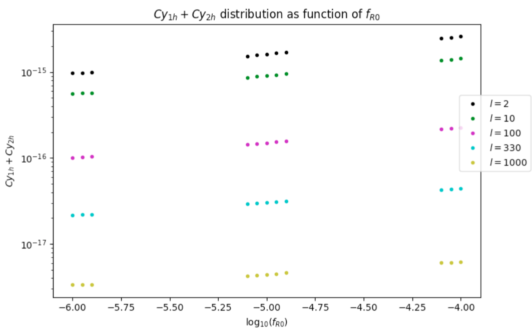

Figure 7.2: SZ Power Spectrum $Cy_{1h} + Cy_{2h}$ values calculated for the values of f_{R0} plotted.

our derivative around $f_{R0} = 10^{-4}$ we use the C_l at $f_{R0} = 10^{-4.05}$. Similarly for derivative around $f_{R0} = 10^{-6}$ we use the C_l at $f_{R0} = 10^{-5.95}$. We compute a one-sided derivative defined as:

$$f'(x) = \frac{f(x+h) - f(x)}{h} + \mathcal{O}(h) \tag{7.5}$$

where $\mathcal{O}(h)$ is the order of error in this definition. For $f_{R0} = 10^{-5}$, we compute a two-sided derivative using the C_l at $f_{R0} = 10^{-4.95}$ and $10^{-5.05}$, defined as:

$$f'(x) = \frac{f(x+h) - f(x-h)}{2h} + \mathcal{O}(h^2) \tag{7.6}$$

Using this method, we get the S/N shown in the Table 7.2:

f_{R0}	CVLE	PRISM	PIXIE
10^{-4}	323.939	49.558	4.954
10^{-5}	415.662	55.847	4.172
10^{-6}	104.324	20.901	1.352

Table 7.2: S/N calculated from Fisher forecast for different f_{R0} parameter values for up-coming PRISM and PIXIE experiments. CVLE refers to a cosmic variance limited experiment.

As we can see, the S/N is high enough to be detected by experiments like PRISM and PIXIE in the future. We confirmed the stability of our result by computing the derivatives using the other f_{R0} values shown in Figure 7.2.
In Figure 7.3, we also plot the contribution towards S/N of every multipole l for the three experiments.

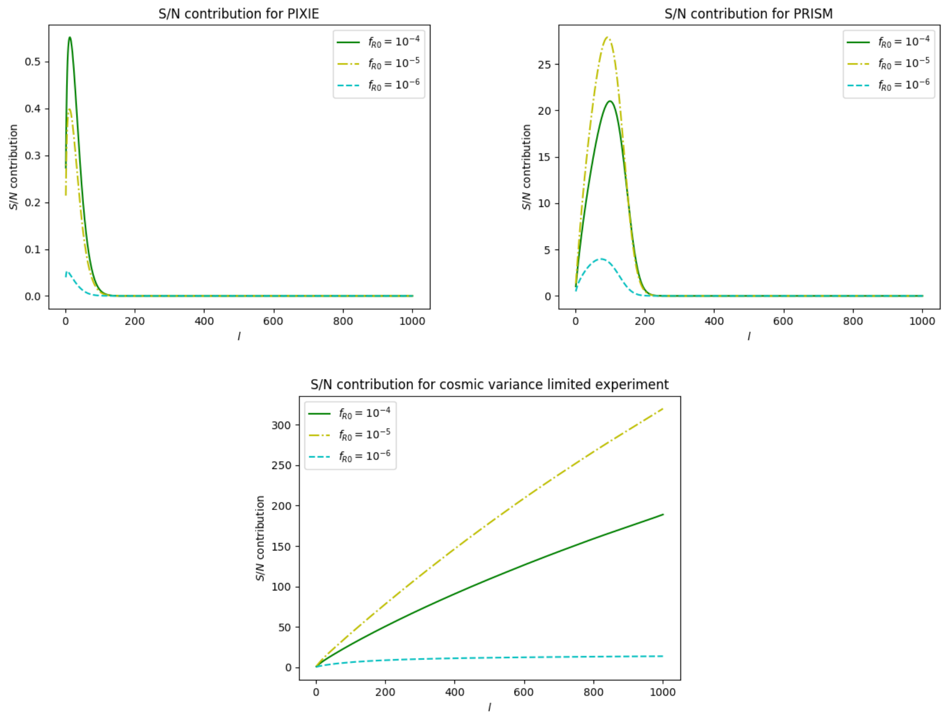

Figure 7.3: Contribution towards S/N as a function of l.

As we can see, the S/N is considerably lower at higher multipoles. This is partly due to higher experimental noise at high multipoles and partly due to the fact that at higher multipoles (small scales), f(R) gravity behaves similar to GR. Note that $f_{R0} = 10^{-5}$ gives the highest S/N for PRISM. This is most probably due to the mass-dependence of R^{sx} for different f_{R0} values as is evident from Figure 6.5. We see that the power gets shifted towards lower mass clusters for $f_{R0} = 10^{-5}$. The S/N here depends on the rate of change of the power spectrum with respect to the total power spectrum, as evident from Eq. 7.2. For $f_{R0} = 10^{-6}$, both factors are small but the rate is smaller; for $f_{R0} = 10^{-4}$ the rate of change is higher but it also has the biggest power spectrum, as clear from Figure 6.7. For $f_{R0} = 10^{-5}$, there is a sweet spot with intermediate power spectrum but higher rate of change, leading to a higher S/N.

Chapter 8

Conclusions

Testing modified gravity models is a highly complicated task, because it is often difficult to calculate accurate predictions for observable quantities. In this thesis, we investigated the imprint of $f(R)$ modified gravity model on the Sunyaev-Zel'dovich power spectrum, and we forecasted its detectability with the next generation of CMB experiments. we used the linear threshold for collapse δ_c calculated numerically by Kopp et. al. [3], for Hu-Sawicki parameteriztion of $f(R)$ modified gravity model [4]. Using the spherical collapse δ_c of $f(R)$ gravity and a drifting diffusing barrier in the excursion set approach, we compute the halo mass functions using the formalism developed in [3] where they showed $n(M, z, f_{R0})$ to be in excellent agreement with numerical Monte Carlo random walk simulations, and applied to generic barriers that are algebraic functions of the variance. Two new parameters were introduced: β takes into account the deviations from spherical collapse and D_B quantifies the scatter around it. We used this formalism to model an aspherical collapse and computed the halo mass function for it, which in turn modified our thermal-SZ autocorrelation power spectrum for different f_{R0} model parameter values. We saw a considerable modification, that motivated a Fisher forecast for this signal in future experiments. The Fisher forecasts gave us a high enough S/N to motivate further work in this area. The existence of substructures within the halo progenitor influences the chameleon effect. This has not been considered in our work since it further complicates the computation of halo mass functions. Therefore, more work is required to fully understand aspherical collapse and all effects of modified gravity on the multiplicity function. We would also like to point out that modification to the halo bias and pressure profile have not been considered in this work. A thorough consideration of all these factors would be the next step in this direction. It would be even better to have modified gravity N-body simulations to measure the collapse parameters.

Bibliography

[1] F. Schmidt, M. Lima, H. Oyaizu, and W. Hu. Phys. Rev. D , 79(8):083518, April 2009. doi: 10.1103/PhysRevD.79.083518.

[2] I. Achitouv, M. Baldi, E. Puchwein, and J. Weller. Phys. Rev. D , 93(10):103522, May 2016. doi: 10.1103/PhysRevD.93.103522.

[3] M. Kopp, S. A. Appleby, I. Achitouv, and J. Weller. Phys. Rev. D , 88(8):084015, October 2013. doi: 10.1103/PhysRevD.88.084015.

[4] W. Hu and I. Sawicki. Phys. Rev. D , 76 (6):064004, September 2007. doi: 10.1103/PhysRevD.76. 064004.

[5] A. A. Starobinsky. Soviet Journal of Experimental and Theoretical Physics Letters, 86:157?163, October 2007. doi: 10.1134/S0021364007150027.

[6] L. Lombriser, B. Li, K. Koyama, and G.-B. Zhao. Phys. Rev. D , 87(12):123511, June 2013. doi: 10.1103/PhysRevD.87.123511.

[7] E. Puchwein, M. Baldi, and V. Springel. MN- RAS, 436:348?360, November 2013. doi: 10.1093/mnras/ stt1575.

[8] F. Schmidt, A. Vikhlinin, and W. Hu. Phys. Rev. D , 80(8):083505, October 2009. doi: 10.1103/PhysRevD.80.083505.

[9] Matteo Cataneo, David Rapetti, Lucas Lombriser, Baojiu Li: ArXiv e-prints (2017), arXiv:1607.08788v2 [astro-ph.CO]

[10] L. Lombriser, A. Slosar, U. Seljak, and W. Hu. Phys. Rev. D , 85(12):124038, June 2012. doi: 10.1103/PhysRevD.85.124038.

[11] William H. Press and Paul Schechter. Astrophys. J., 187:425?438, 1974. doi: 10.1086/152650.

[12] J. Tinker, A. V. Kravtsov, A. Klypin, K. Abazajian, M. Warren, G. Yepes, S. Gottlober, and D. E. Holz. The Limits of Universality. Astrophys. J. , 688:709-728, De- cember 2008. doi: 10.1086/591439.

[13] A. G. Riess, et. al. Astronomical Journal, 116, 1009 (1998), arXiv:astro-ph/9805201.

[14] S. Perlmutter, et. al. Astrophysical Journal, 517, 565 (1999), arXiv:astro-ph/9812133.

[15] J. Khoury and A. Weltman, Physical Review D, 69, 044026 (2004), arXiv:astro-ph/0309411.

[16] F. Schmidt, M. Lima, H. Oyaizu, and W. Hu, Physical Review D, 79, 083518 (2009), arXiv:0812.0545.

[17] I. Achitouv, Y. Rasera, R. K. Sheth, and P. S. Corasaniti, ArXiv e-prints (2012), arXiv:1212.1166 [astro-ph.CO].

[18] Navarro, J. F., Frenk, C. S., & White, S. D. M. 1997, ApJ, 490, 493

[19] Duffy, A. R., Schaye, J., Kay, S. T., & Dalla Vecchia, C. 2008, MNRAS, 390, L64

[20] Chandrasekhar, S., 1950. Radiative Transfer, New York:Dover

[21] Wright, E.L., 1979. ApJ, 232, 348

[22] Limber, D. N. 1954, ApJ, 119, 655

[23] Berkinshaw, 1998. arxiv.org/pdf/astro-ph/9808050.pdf

[24] Cooray, A., Sheth, R. 2002 arxiv.org/pdf/astro-ph/0206508.pdf

[25] Komatsu, E., & Seljak, U. 2002, MNRAS, 336, 1256

[26] Tinker, J. L., et. al. ArXiv e-prints (2010), arXiv:1001.3162 [astro-ph.CO].

[27] Felice, A., Tsujikawa, S. ArXiv e-prints (2010), arXiv:1002.4928 [gr-qc].

[28] S. Ferraro, F. Schmidt, W. Hu ArXiv e-prints (2010), arXiv:1011.0992 [astro-ph.CO].

[29] Battaglia, N., Bond, J. R., Pfrommer, C., & Sievers, J. L. 2012, ApJ, 758, 75

[30] Battaglia, N., Bond, J. R., Pfrommer, C., Sievers, J. L., & Sijacki, D. 2010, ApJ, 725, 91

[31] R. Ferraro. ArXiv e-prints (2012), arXiv:1204.6273 [gr-qc].

[32] Hill, J. C., Pajer, E. ArXiv e-prints (2013), arXiv:1303.4726 [astro-ph.CO].

[33] I. Achitouv, Y. Rasera, R.K. Sheth, P.S. Corasaniti. ArXiv e-prints (2014), arXiv:1212.1166 [astro-ph.CO].

[34] Koyama, K. ArXiv e-prints (2016), arXiv:1504.04623 [astro-ph.CO].

[35] Peirone, S., Raveri, M., et. al. ArXiv e-prints (2016), arXiv:1607.07863 [astro-ph.CO]

[36] A. Heavens. ArXiv e-prints (2010), arXiv:0906.0664v3 [astro-ph.CO]

[37] Planck Collaboration, Ade, P. A. R., Aghanim, N., et al. 2014, arXiv:1303.5076

[38] Planck Collaboration, Ade, P. A. R., Aghanim, N., et al. 2015, arXiv:1502.01589

[39] Copeland, E. J., Sami, M., & Tsujikawa, S. 2006, International Journal of Modern Physics D, 15, 1753, arXiv:hep-th/0603057

[40] Liddle Andrew R. and Lyth David H., The Primordial Density Perturbation, 2010, Cambridge University Press

[41] Hubble, E., Proc.Nat.Ac.Sci. 15, (1929)

[42] Coles Peter and Lucchin Francesco, Cosmology: The Origin and Evolution of Cosmic Structure, 2002, John Wiley Sons Inc Print on

[43] Petschek, A. G. (ed.): 1990, *Supernovae*, Springer, Heidelberg

[44] J. Ganc and E. Komatsu. Phys.Rev. D86 (2012) 023518, [arXiv:1204.4241].

[45] R. Emami, E. Dimastrogiovanni, J. Chluba, and M. Kamionkowski. Phys. Rev. D91 (2015), no. 12 123531, [arXiv:1504.00675].

[46] D. J. Fixsen, E. S. Cheng, J. M. Gales, J. C. Mather, R. A. Shafer, E. L. Wright. ArXiv e-prints (1996), arXiv:astro-ph/9605054

[47] C. Creque-Sarbinowski, S. Bird, and M. Kamionkowski. arXiv:1606.00839 [astro-ph.CO].

[48] T. T. Nakamura and Y. Suto, Progress of Theoretical Physics, 97, 49 (1997), arXiv:astro-ph/9612074.

List of Figures

List of Tables